A protein-based model of carbon monoxide dehydrogenase exhibits tunable covalency across cluster oxidation and ligand-bound states

Luke C. Lewis[a], Prajakta Badve[c], Itzel P. Vaca[b], Pujan Ajmera[b], Yuri Lee,[b] Anastassia N. Alexandrova[b], Katlyn K. Meier[c], Hannah S. Shafaat[a,b*]

a – Department of Chemistry and Biochemistry, The Ohio State University, Columbus, Ohio 43210, United States
b – Department of Chemistry and Biochemistry, University of California Los Angeles, Los Angeles, California 90095, United States
c – Department of Chemistry, University of Miami, Cox Science Center, 1301 Memorial Drive, Coral Gables, Florida 33146, United States

Supplementary Information

Table of Contents

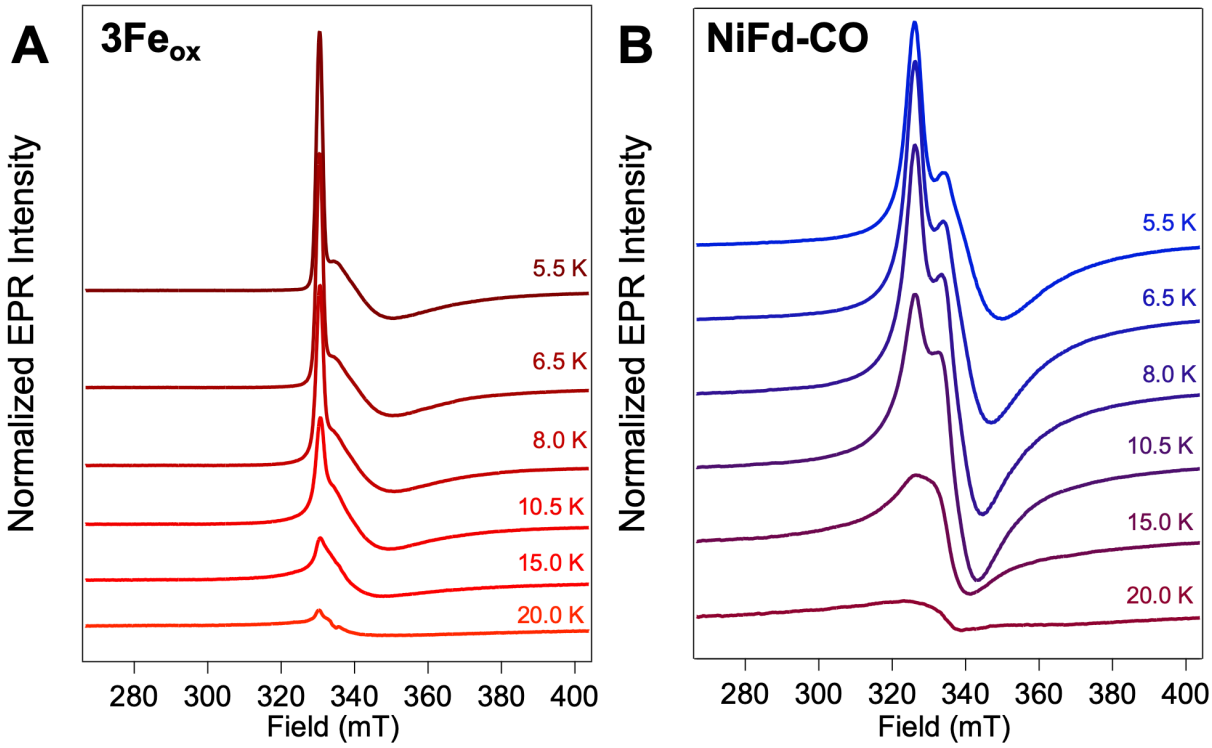

Figure S1. CW EPR spectra (ν = 9.37 GHz) of (A) $[Fe_3S_4]^+$ Fd, $P_{\mu w}$ = 0.2 mW and (B) NiFd-CO, $P_{\mu w}$ = 20 mW at indicated temperatures. Spectra were normalized to temperature using the typical Curie dependence [I x T], which highlights the lineshape differences induced by raising the temperature.

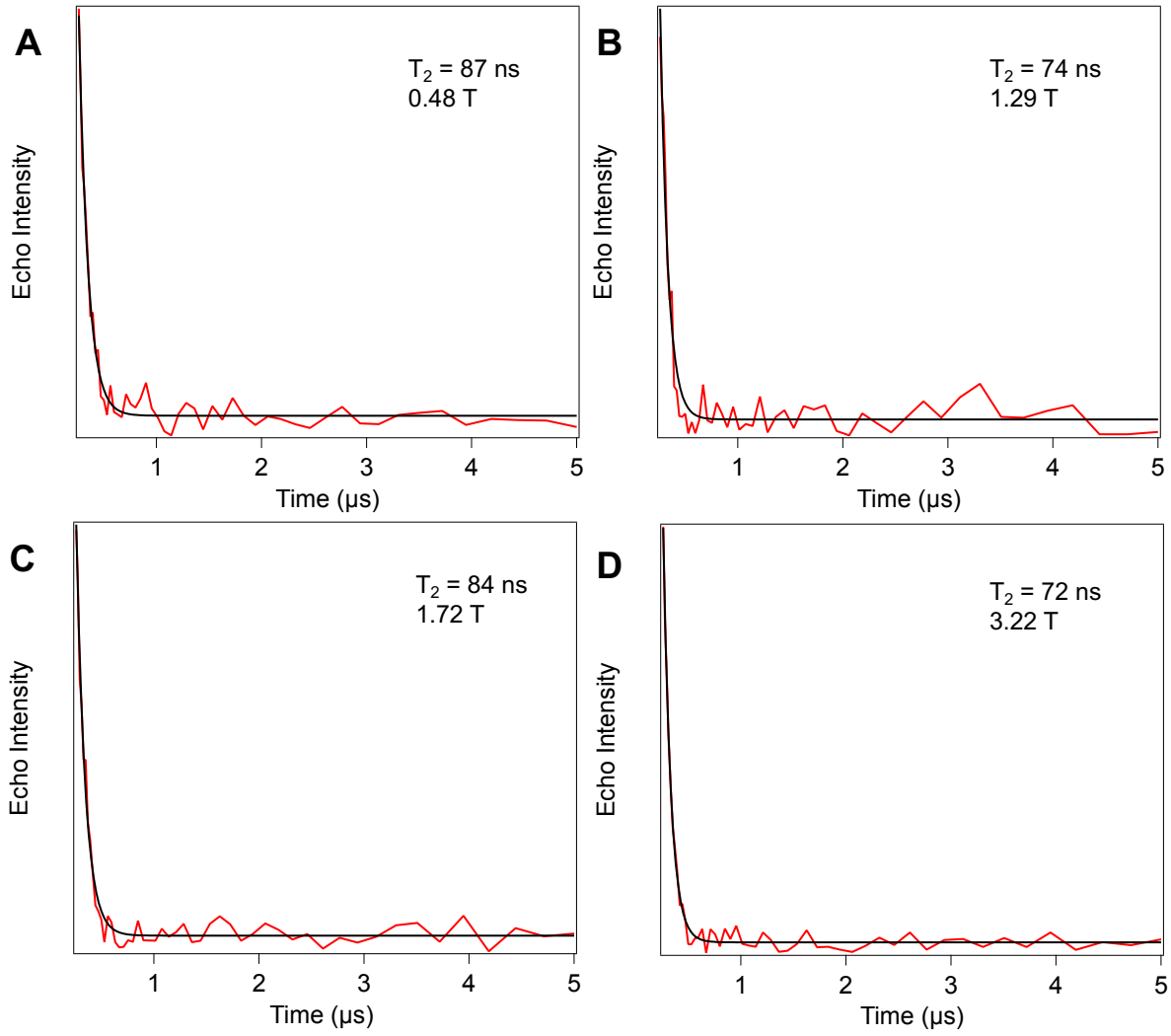

Figure S2. Experimental T_2 relaxation experiments (*red*) overlaid with exponential fit (*black*) of $NiFd_{red}$ at (**A**) B_0 = 0.48 T, (**B**) 1.29 T, (**C**) 1.72 T, (**D**) 3.22 T. Experimental conditions: $\pi/2$ = 32 ns, τ = 260 ns, Temperature = 5 K.

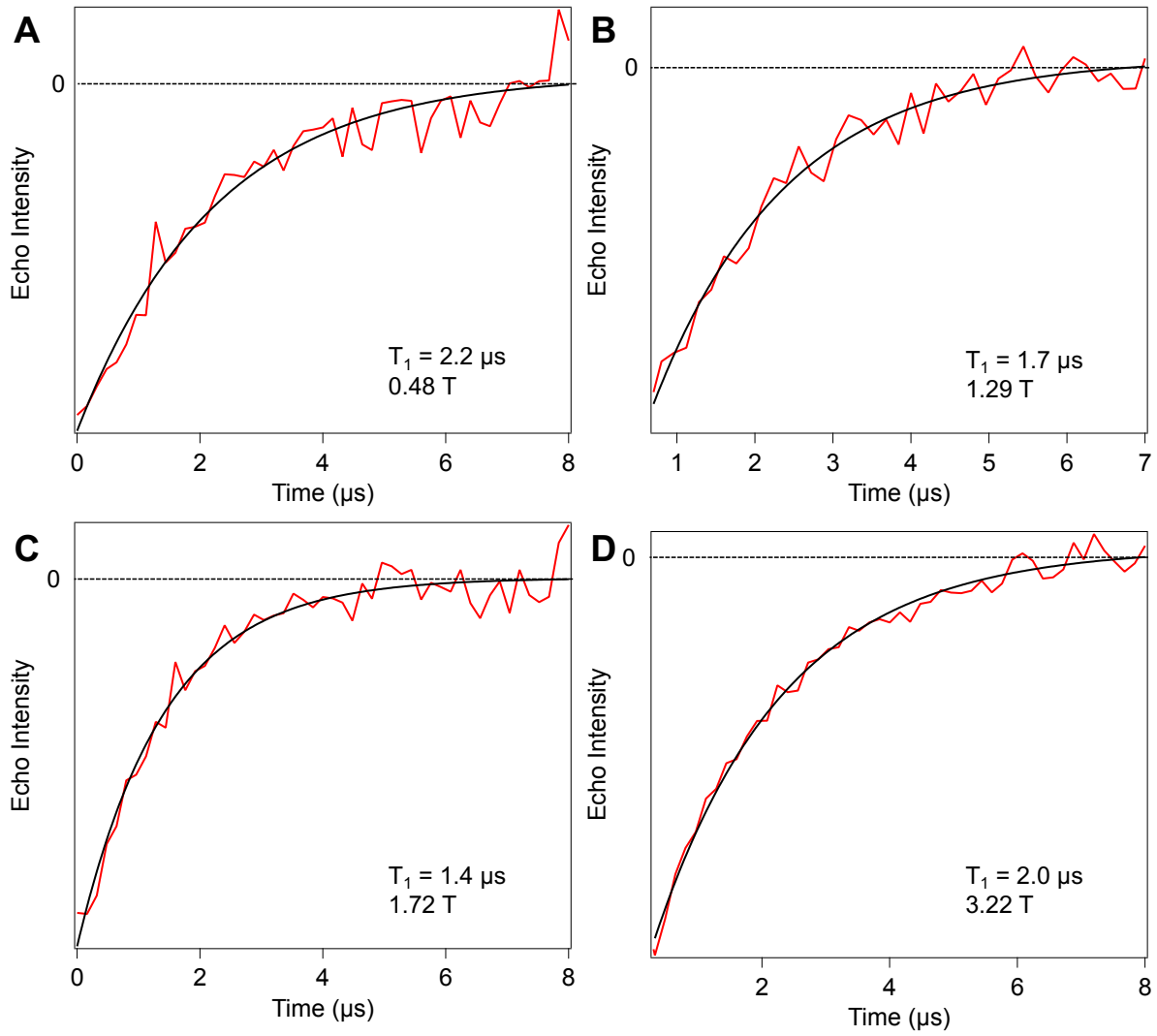

Figure S3. Experimental T_1 relaxation experiments (*red*) overlaid with fit (*black*) of $NiFd_{red}$ at (**A**) B_0 = 0.48 T, (**B**) 1.29 T, (**C**) 1.72 T, (**D**) 3.22 T. Dashed line at 0 included for reference. Experimental conditions: $\pi/2$ = 32 ns, τ = 260 ns, T = 25 µs, Temperature = 5 K.

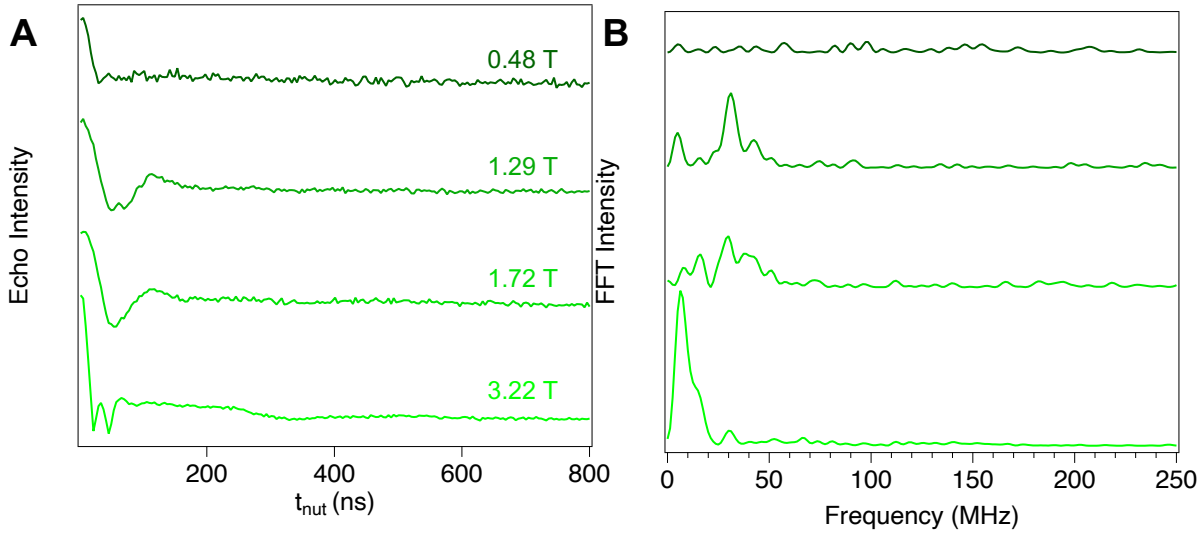

Figure S4. Nutation experiments of $NiFd_{red}$ at indicated field positions in (**A**) the time domain and (**B**) the corresponding Fourier transform. Experimental conditions: $\pi/2$ = 32 ns τ = 260 ns, Temperature = 5 K.

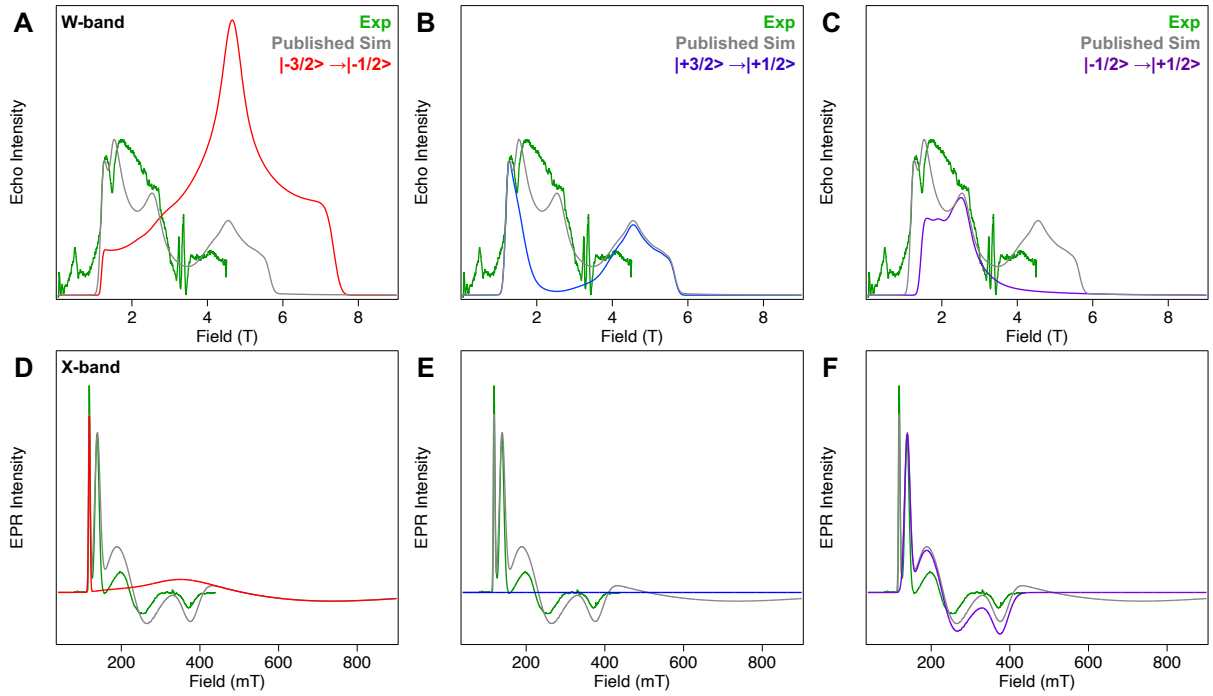

Figure S5. (**A-C**) Experimental (*green*) and simulated (*gray*) W-band (ν = 94 GHz) EDFS EPR spectra and (**D-F**) X-band CW EPR spectra of $NiFd_{red}$. Signals corresponding to the transitions from $m_s = -3/2 \rightarrow m_s = -1/2$ (*red*), $m_s = +3/2 \rightarrow m_s = +1/2$ (*blue*), and $m_s = -1/2 \rightarrow m_s = +1/2$ (*purple)* are displayed for reference. The best fit was provided using the simulated parameters $S_{tot} = 3/2$, $g_1, g_2, g_3 = 1.92, 1.97, 1.93$, $D = -2.495$ cm^{-1}, and $|E/D| = 0.17$, excluding the $m_s = -3/2 \rightarrow m_s = -1/2$ transition at W-band due to relaxation effects.

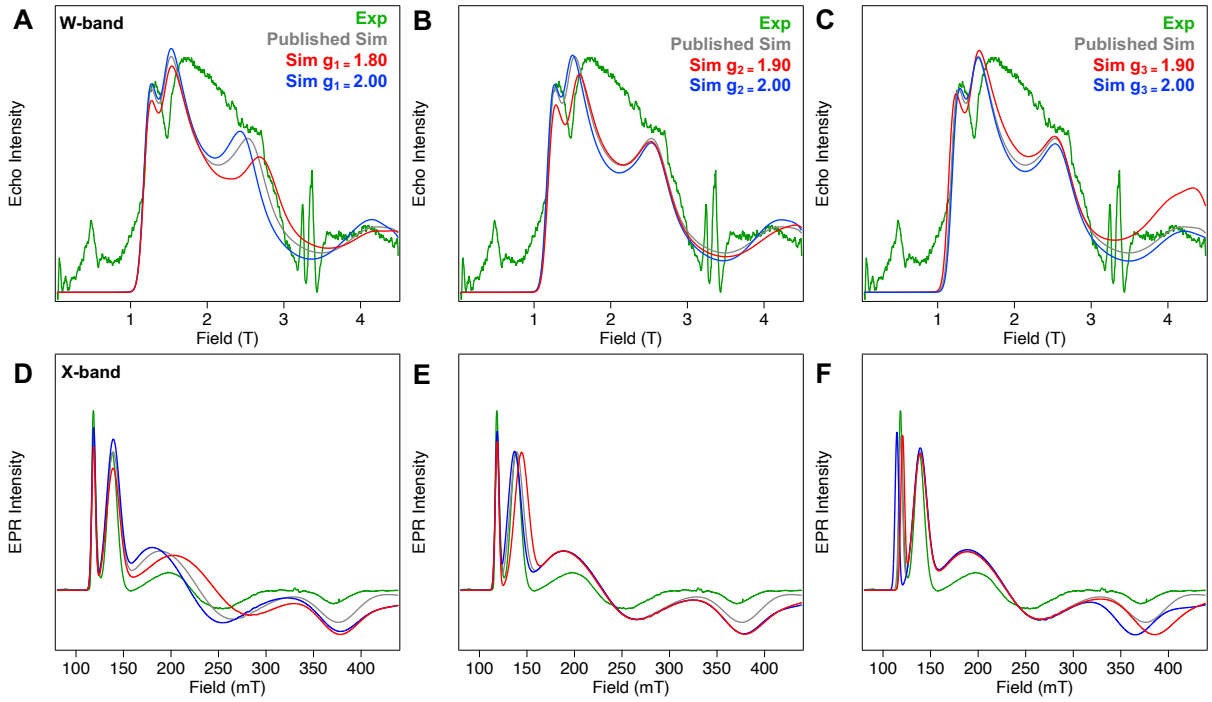

Figure S6. (**A-C**) Experimental (*green*) and simulated (*gray*) W-band (ν = 94 GHz) EDFS EPR spectra and (**D-F**) X-band CW EPR spectra of $NiFd_{red}$. Alternative simulated parameters for g_1 (**A/D**), g_2 (**B/E**), and g_3 (**C/F**) are shown for clarity. The best fit was provided using the simulated parameters S_{tot} = 3/2, g_1, g_2, g_3 = 1.92, 1.97, 1.93, D = -2.495 cm^{-1}, and |E/D| = 0.17

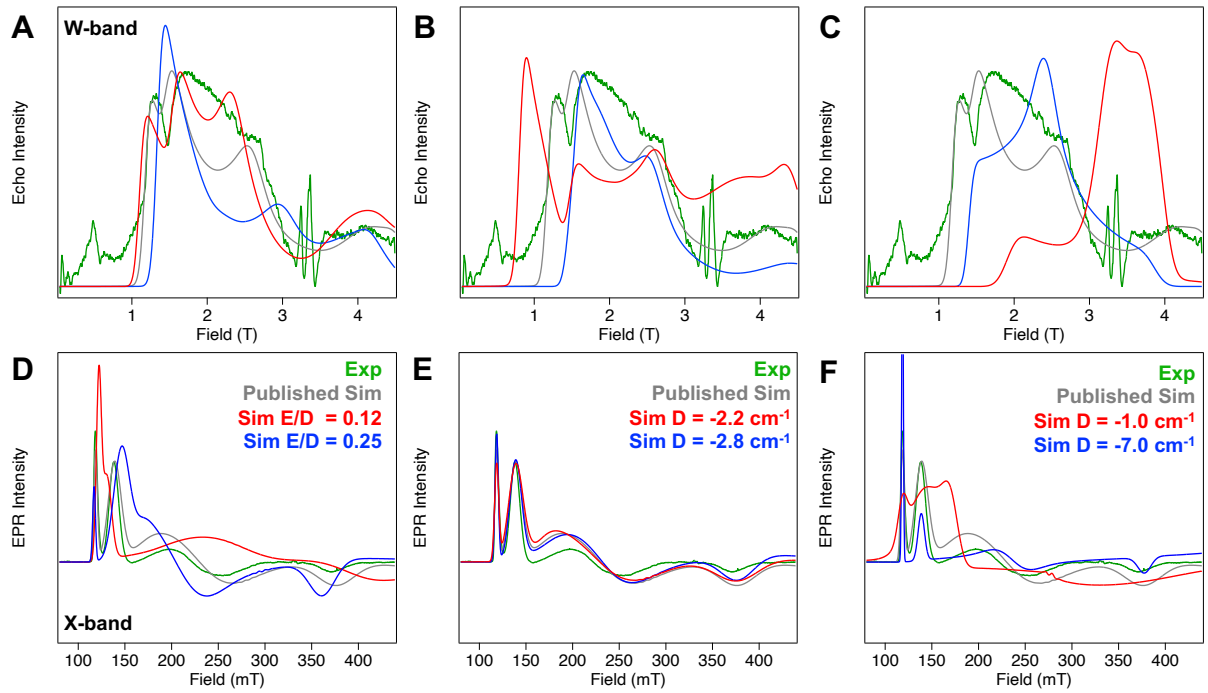

Figure S7. (**A-C**) Experimental (*green*) and simulated (*gray*) W-band (ν = 94 GHz) EDFS EPR spectra and (**D-F**) X-band (ν = 9.37 GHz) CW EPR spectra of $NiFd_{red}$. Alternative simulated parameters for E/D (**A/D**), and the magnitude of the zero-field splitting, *D*, (**B-F**) are shown for clarity. The best fit was provided using the simulated parameters $S_{tot} = 3/2$, g_1, g_2, $g_3 = 1.92, 1.97, 1.93$, $D = -2.495\ cm^{-1}$, and $|E/D| = 0.17$

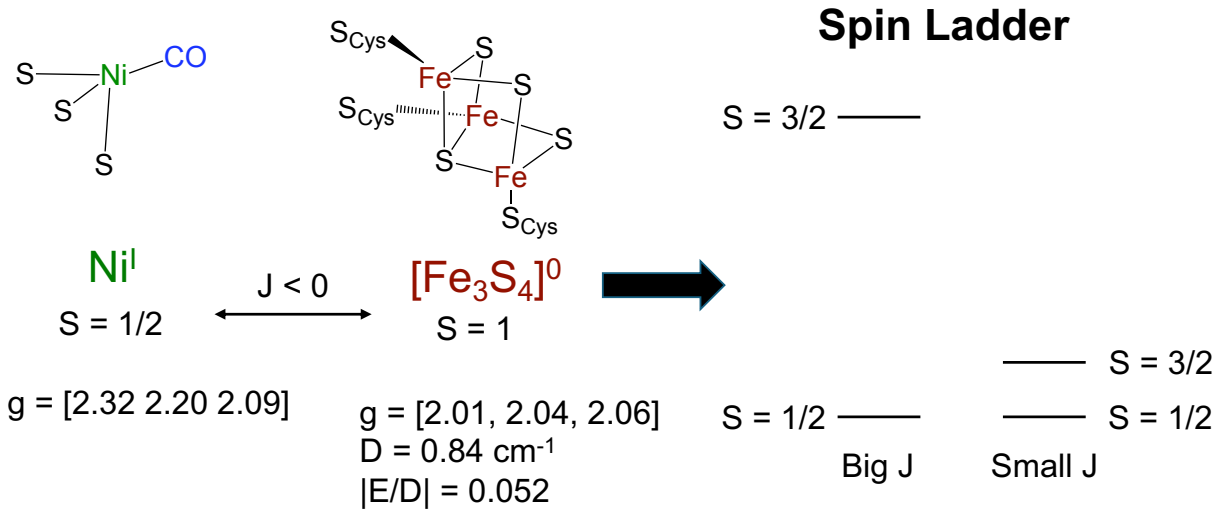

Figure S8. Representative coupling scheme for NiFd-CO indicating how the magnitude of the exchange coupling (J) changes the relative energy gap between the ground and excited state.

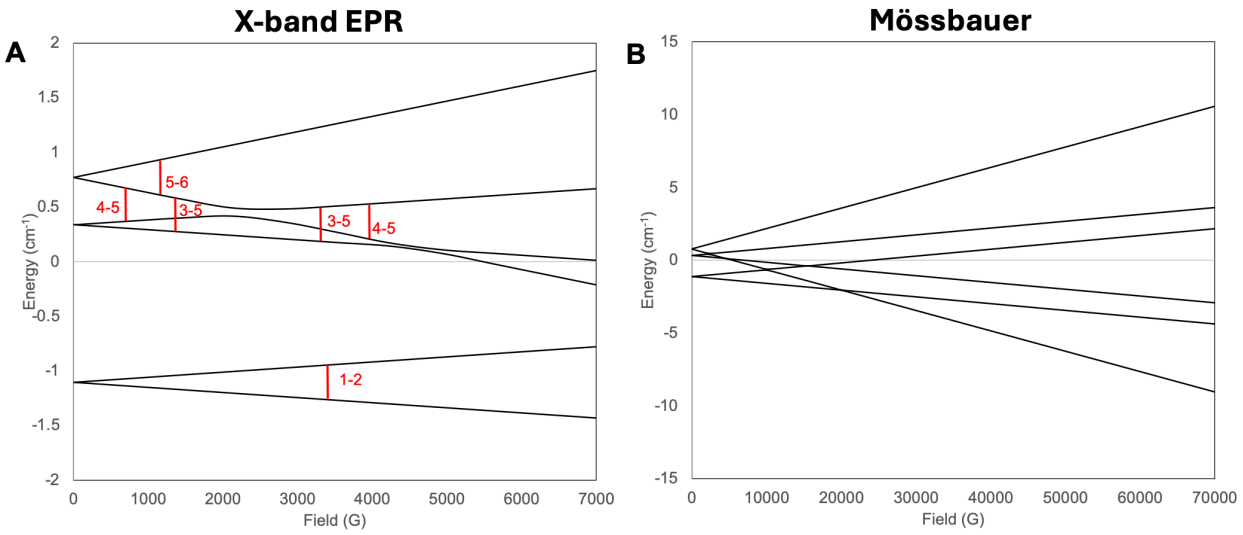

Figure S9. Energy level diagrams of NiFd-CO in both (**A**) EPR and (**B**) Mössbauer energy regimes**.**

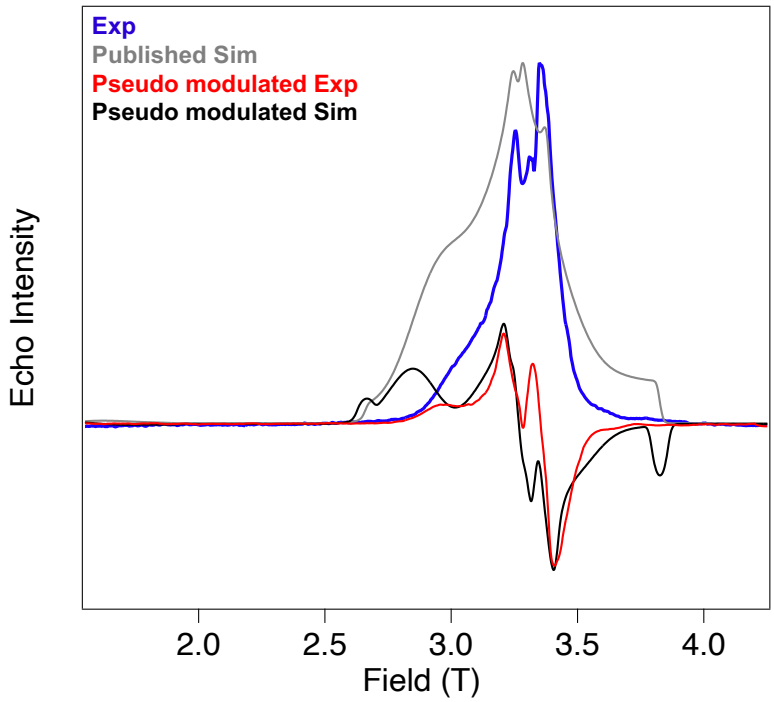

Figure S10. Experimental (*blue*) and simulated (*gray*) W-band EDFS EPR spectrum (T = 5 K) of NiFd-CO with the experimental (red) and simulated (black) pseudo-modulated spectra for clarity. Simulations were performed assuming a spin-coupled system with $S_{1,Fe3}$ = 1, g_1, g_2, g_3 = [2.01, 2.04, 2.06], D = 0.84 cm^{-1}, E/D = 0.052; and $S_{2,Ni}$ = ½, g_1, g_2, g_3 = [2.32, 2.20, 2.09], with an exchange coupling J = -1.0 cm^{-1}. The resulting spin ladder predicts 44 % population of the S = ½ spin level (g_1, g_2, g_3 = 1.91, 1.99, 2.05) and 56 % of the S = 3/2 spin level (g_1, g_2, g_3 = 2.12, 2.09, 2.07; D_1, D_2, D_3 (MHz) = -2361, -3234, 5596] at 5 K.

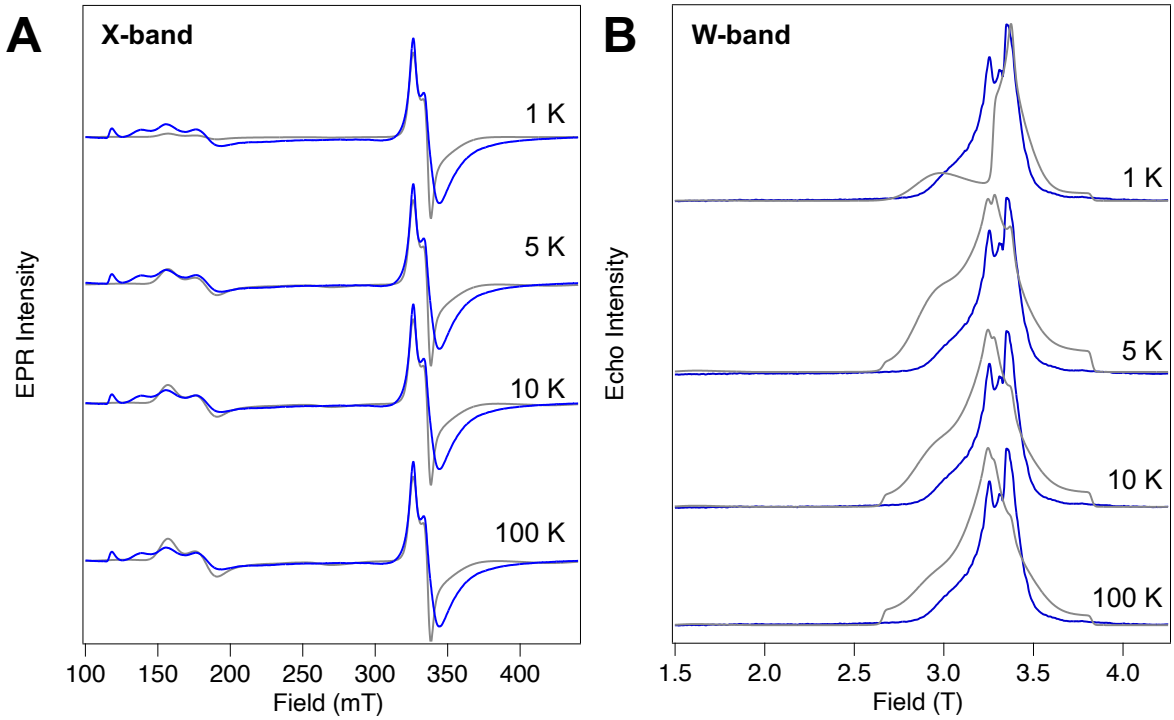

Figure S11. Experimental (*blue*) and simulated (*gray*) (**A**) X-band CW EPR spectrum of NiFd-CO (T = 8 K) and (**B**)W-band EDFS EPR spectra (T = 5 K). Experimental spectra are presented for only one temperature. Simulations were performed assuming a spin-coupled system at variable indicated temperatures with $S_{1,Fe3}$ = 1, g_1, g_2, g_3 = [2.01, 2.04, 2.06], D = 0.84 cm^{-1}, E/D = 0.052; and $S_{2,Ni}$ = ½, g_1, g_2, g_3 = [2.32, 2.2, 2.09], with an exchange coupling J = -1.0 cm^{-1}. The resulting spin ladder predicts the populations of the corresponding S = ½ and S = 3/2 energy levels.

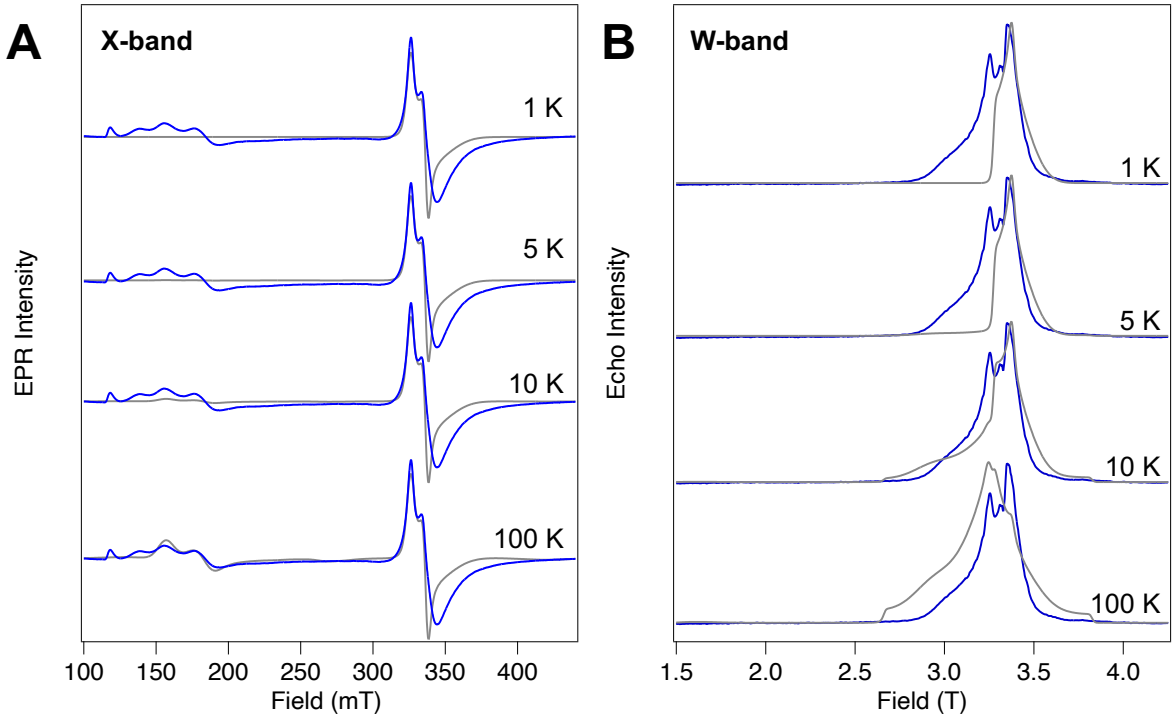

Figure S12. Experimental (*blue*) and simulated (*gray*) (**A**) X-band CW EPR spectrum of NiFd-CO (T = 8 K) and (**B**)W-band EDFS EPR spectra (T = 5 K). Experimental spectra are presented for only one temperature. Simulations were performed assuming a spin-coupled system at variable indicated temperatures with $S_{1,Fe3}$ = 1, g_1, g_2, g_3 = [2.01, 2.04, 2.06], D = 0.84 cm^{-1}, E/D = 0.052; and $S_{2,Ni}$ = ½, g_1, g_2, g_3 = [2.32, 2.2, 2.09], with an exchange coupling J = -10 cm^{-1}. The resulting spin ladder predicts the populations of the corresponding S = ½ and S = 3/2 energy levels.

Temperature (K)	% Population S = 1/2	% Population S = 3/2
1	83	17
5	44	56
10	39	61
15	37	63
100	34	66
1000	33	67

J = -1.0 cm^{-1}

Temperature (K)	% Population S = 1/2	% Population S = 3/2
1	100	0.0
5	98	2.0
10	83	17
15	69	31
100	39	61
1000	34	66

J = -10 cm^{-1}

Table S1. Relative populations of the ground state (S = ½) and excited state (S = 3/2) for NiFd-CO at different temperatures using the spin ladder model, $J_{Ni\text{-}Fe3}$ = -1.0 cm^{-1} and -10 cm^{-1}.

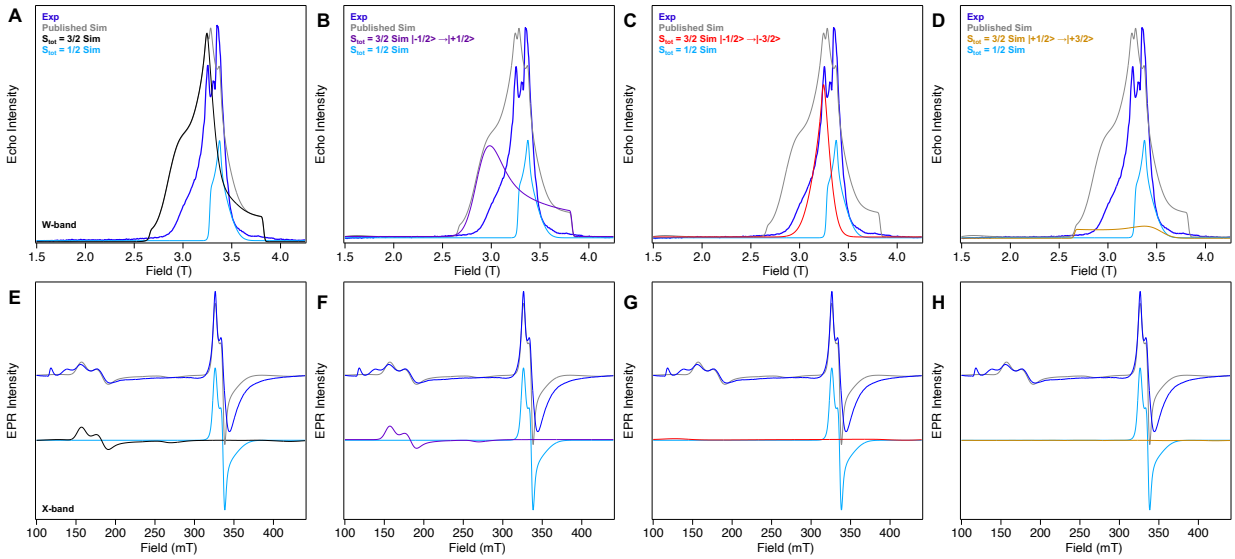

Figure S13. (**A-D**) Experimental (*blue*) and simulated (*gray*) W-band (ν = 94 GHz, T = 5 K) EDFS EPR spectra and (**E-H**) X-band (ν = 9.37 GHz, T = 8 K) CW EPR spectra of NiFd-CO. Signals corresponding to the S = 3/2 (*black*) and S = ½ (*cyan*) spin levels (**A/E**), and transitions from m_s =-1/2 → m_s = +1/2 (*purple*), m_s = -1/2 → m_s = -3/2 (*red*), and m_s = +1/2 → m_s = +3/2 (*yellow)* are displayed for reference. The best model of the data assumed a spin-coupled system with $S_{1,Fe3}$ = 1, g_1, g_2, g_3 = [2.01, 2.04, 2.06], D = 0.84 cm^{-1}, E/D = 0.052; and $S_{2,Ni}$ = ½, g_1, g_2, g_3 = [2.32, 2.20, 2.09], with an exchange coupling J = -1.0 cm^{-1}. The resulting spin ladder predicts a S = ½ spin level (g_1, g_2, g_3 = 1.91, 1.99, 2.05) and a S = 3/2 spin level (g_1, g_2, g_3 = 2.12, 2.09, 2.07; D_1, D_2, D_3 = -2361, -3234, 5596 MHz).

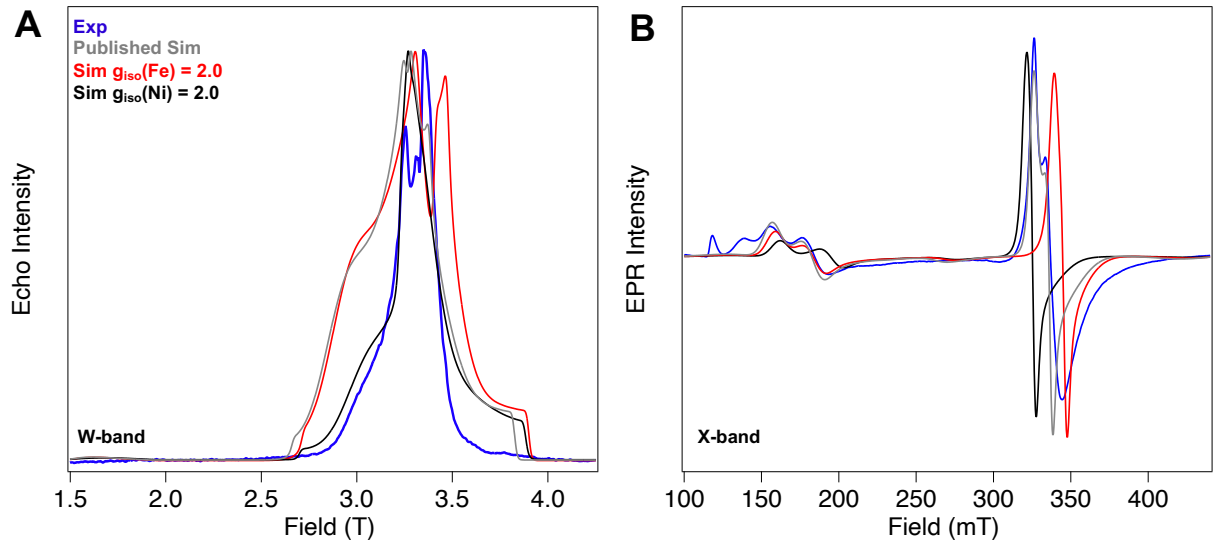

Figure S14. (**A**) Experimental (*blue*) and simulated (*gray*) W-band (ν = 94 GHz, T = 5 K) EDFS EPR spectra and (**B**) X-band (ν = 9.37 GHz, T = 8 K) CW EPR spectra of NiFd-CO. Alternative simulated parameters assuming a g_{iso} = 2.0 for $S_{1,Fe3}$ (*red*) and a g_{iso} = 2.0 for $S_{2,Ni}$ (*black*) are shown for reference. The best model of the data assumed a spin-coupled system with $S_{1,Fe3}$ = 1, g_1, g_2, g_3 = [2.01, 2.04, 2.06], D = 0.84 cm^{-1}, E/D = 0.052; and $S_{2,Ni}$ = ½, g_1, g_2, g_3 = [2.32, 2.20, 2.09], with an exchange coupling J = -1.0 cm^{-1}. The resulting spin ladder predicts a S = ½ spin level (g_1, g_2, g_3 = 1.91, 1.99, 2.05) and a S = 3/2 spin level (g_1, g_2, g_3 = 2.12, 2.09, 2.07; D_1, D_2, D_3 (MHz) = -2361, -3234, 5596).

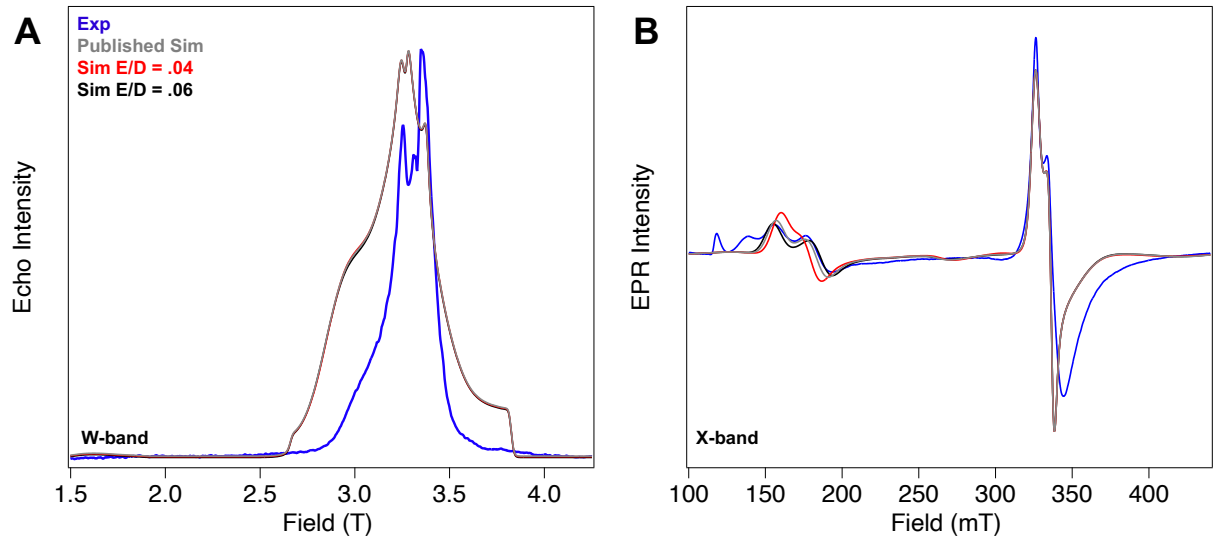

Figure S15. Experimental (*blue*) and simulated (*gray*) (**A**) W-band EDFS EPR spectrum (T = 5 K) and (**B**) X-band CW EPR spectrum of NiFd-CO (T = 8 K). Alternative simulated parameters assuming an |E/D| = 0.04 (*red*) and |E/D| = 0.06 (*black*) for the iron subcluster, $S_{1,Fe}$ are shown for reference. The best model of the data assumed a spin-coupled system with $S_{1,Fe3}$ = 1, g_1, g_2, g_3 = [2.01, 2.04, 2.06], D = 0.84 cm^{-1}, E/D = 0.052; and $S_{2,Ni}$ = ½, g_1, g_2, g_3 = [2.32, 2.20, 2.09], with an exchange coupling J = -1.0 cm^{-1}. The resulting spin ladder predicts a S = ½ spin level (g_1, g_2, g_3 = 1.91, 1.99, 2.05) and a S = 3/2 spin level (g_1, g_2, g_3 = 2.12, 2.09, 2.07; D_1, D_2, D_3 (MHz) = -2361, -3234, 5596).

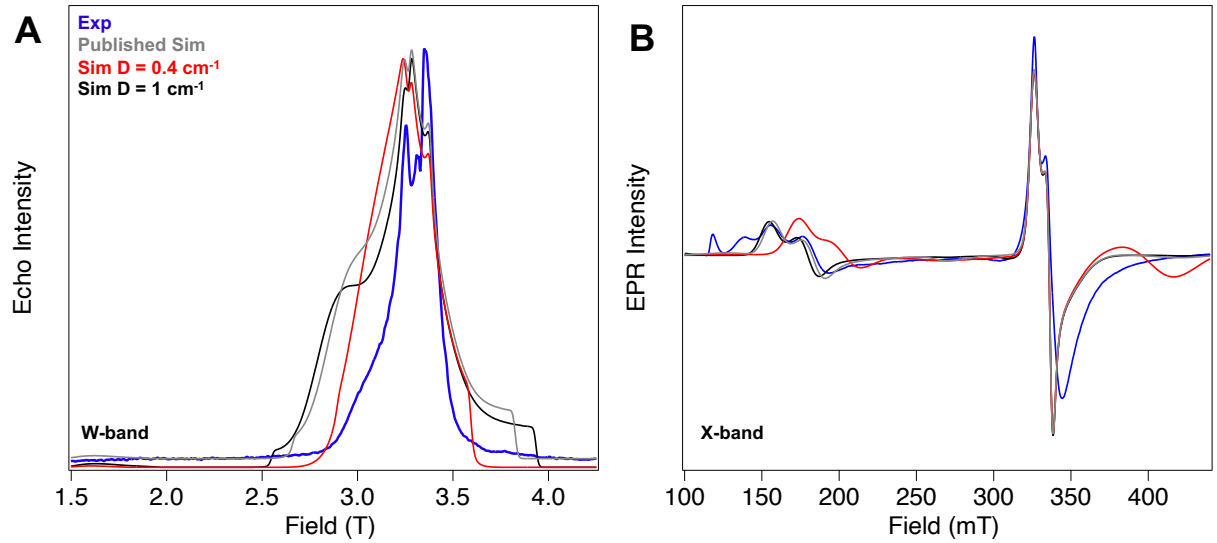

Figure S16. Experimental (*blue*) and simulated (*gray*) (**A**) W-band EDFS EPR spectrum (T = 5 K) and (**B**) X-band CW EPR spectrum of NiFd-CO (T = 8 K). Alternative simulated parameters assuming a zero-field splitting, D = 0.4 cm^{-1} (*red*) and D = 1.0 cm^{-1} (*black*) for the iron subcluster, $S_{1,Fe}$ are shown for reference. The best model of the data assumed a spin-coupled system with $S_{1,Fe3}$ = 1, g_1, g_2, g_3 = [2.01, 2.04, 2.06], D = 0.84 cm^{-1}, E/D = 0.052; and $S_{2,Ni}$ = ½, g_1, g_2, g_3 = [2.32, 2.20, 2.09], with an exchange coupling J = -1.0 cm^{-1}. The resulting spin ladder predicts a S = ½ spin level (g_1, g_2, g_3 = 1.91, 1.99, 2.05) and a S = 3/2 spin level (g_1, g_2, g_3 = 2.12, 2.09, 2.07; D_1, D_2, D_3 (MHz) =[-2361, -3234, 5596).

	Experimental		Calculated	
Temperature (K)	**%S = 1/2**	**% S = 3/2**	**%S = 1/2**	**% S = 3/2**
4.0	52	48	46	54
4.5	44	56	45	55
5.5	44	56	43	57
6.5	45	55	41	59
8.0	43	57	40	60
10.5	39	61	38	62
15.0	37	63	37	63

Table S2. Populations of the ground (S = ½) and excited states (S = 3/2) for NiFd-CO at indicated temperatures. Simulated populations were fit to experimental data using Easyspin[1] and compared with calculated populations using the spin ladder model, $J_{Ni\text{-}Fe3}$ = -1.0 cm^{-1}

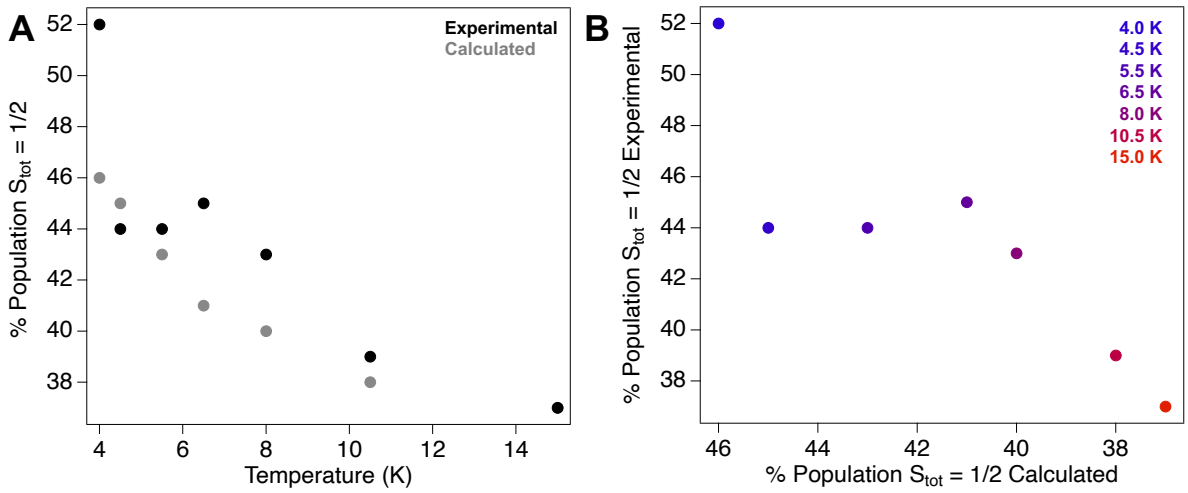

Figure S17. (A) Experimentally determined (*black*) and calculated (*gray*) populations of the S_{tot} = ½ spin level of NiFd-CO as a function of temperature. (**B**) Linear relationship highlighting the correlated between the experimentally determined and calculated populations of the S_{tot} = 1/2 spin level of NiFd-CO at the indicated temperatures.

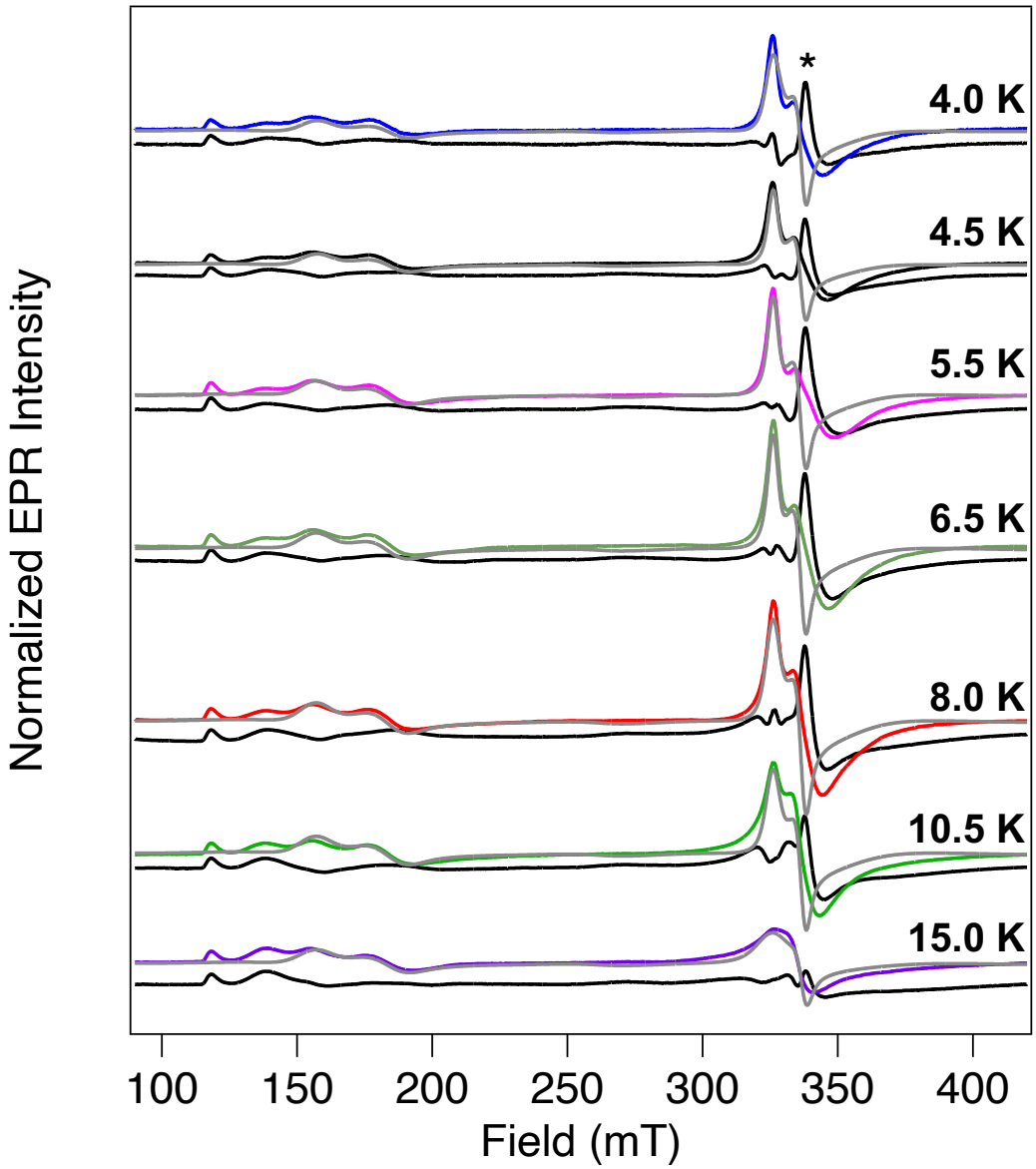

Figure S18. CW EPR spectra (ν = 9.37 GHz) of NiFd-CO at the indicated temperatures. The contribution of S_{tot} = ½ and S_{tot} = 3/2 spin states were fit using Easyspin[1], and the simulated spectra (*gray*) were subtracted from the experimental spectra (*colored*) to generate the residuals (*black*). The * denotes a subtraction artifact due to poor modeling of the lineshape and relaxation characteristics of the high-field side of the S_{tot} = ½ spin level. Residual $NiFd_{red}$ can be seen from 100 – 200 mT. Spectra were normalized to temperature using the typical Curie dependence [I x T].

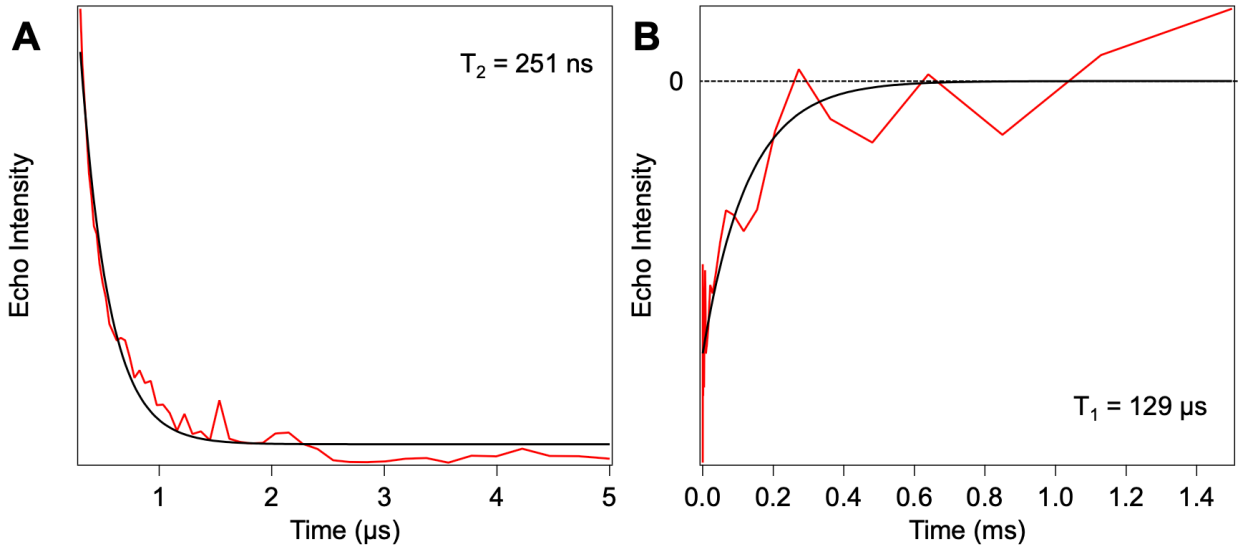

Figure S19. Experimental (**A**) T_2 and (**B**) T_1 relaxation experiments (*red*) overlaid with exponential fit (*black*) of NiFd-CO at T = 5 K and B_o = 3.25 T. Experimental conditions: $\pi/2$ = 32 ns, τ = 260 ns, T = 25 µs (for T_1 measurements), Temperature = 5 K.

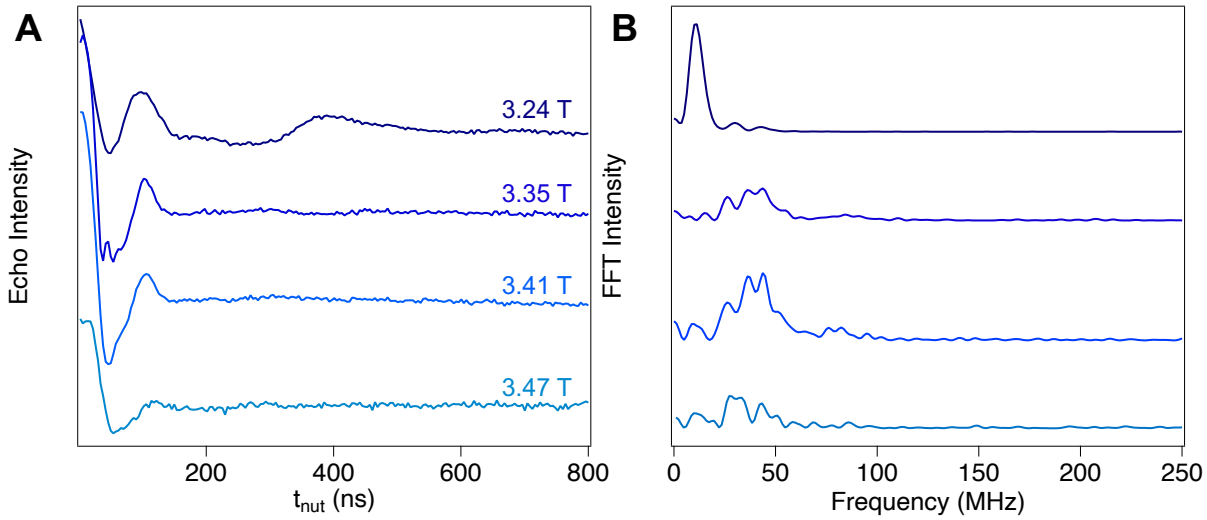

Figure S20. Nutation experiments of NiFd-CO at indicated field positions in (**A**) time domain and (**B**) the corresponding Fourier transform. Experimental conditions: $\pi/2$ = 32 ns, τ = 260 ns, Temperature = 5 K.

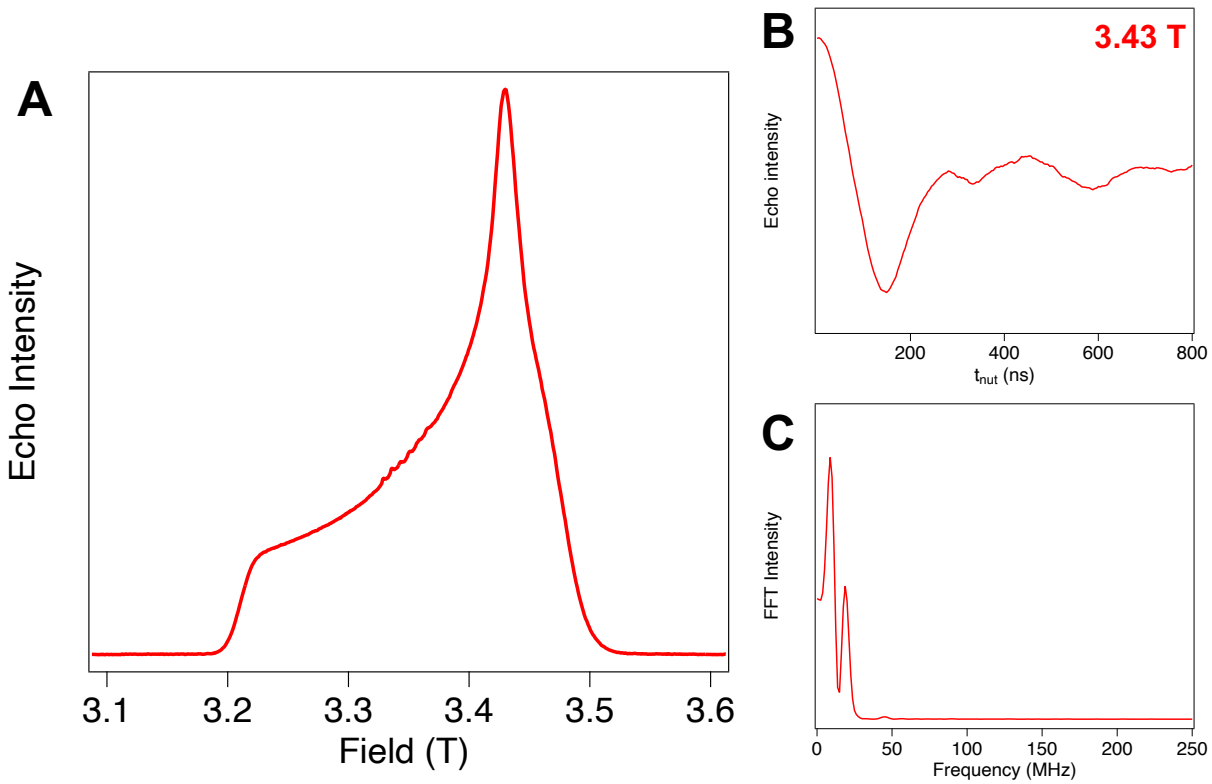

Figure S21. (A) W-band EDFS spectrum of S_{tot} = 1/2 [Fe_4S_4]-CN Fd. Nutation experiments of [Fe_4S_4]-CN Fd at indicated field position in (**A**) time domain and (**B**) the corresponding Fourier transform. Experimental conditions: $\pi/2$ = 32 ns, τ = 260 ns, Temperature = 5 K.

Discussion of $NiFd_{red}$ and NiFd CO EPR Spectral Simulations

$NiFd_{red}$

The X-band (ν = 9.37 GHz) CW EPR spectrum of $NiFd_{red}$ exhibits signal consistent with previously reported spectra by us and others, which best modeled the spectrum as a S_{tot} = 3/2 spin system with g_{iso} = 2.0, |E/D| = 0.16 and zero-field splitting, D = -2.2 cm^{-1}.[2–4] However, at X-band frequencies, the microwave quantum ($\Delta E_{\mu w}$ ~0.3 cm^{-1}) is smaller than D, resulting in a spectrum that is dominated by the zero-field splitting (ZFS) terms and not the electronic Zeeman interaction, precluding assignment of the g-tensor and refinement of the ZFS terms. Acquiring spectra at W-band (ν = 94 GHz, $\Delta E_{\mu w}$ ~ 3 cm^{-1}) allows for additional refinement of the ZFS and g-tensors as the spectrum is now heavily influenced by both the ZFS terms and the Zeeman interaction. It is worth noting that the W-band spectrum was collected as an echo-detected field sweep (EDFS) while the X-band spectrum was collected on a standard continuous-wave (CW) spectrometer. The line shapes and resonant positions of EDFS spectra may be influenced by different relaxation mechanisms and potential electron spin echo envelope modulations (ESEEM), and as such, the intensities of peaks in such spectra may not be well-represented by using a continuous-wave EPR simulation.

We initially performed relaxation and nutation measurements to identify which signals may correspond to the S_{tot} = 3/2 signal (**Figures S2-S4**). The T_1 and T_2 values are all very fast and consistent across the spectral window. Likewise, the nutation frequencies (ν_{nut} ~ 30 MHz) are fairly consistent across the spectral window. However, at B_o = 3.22 T, a low frequency nutation is apparent that may suggest contamination of a lower spin (S = ½) species (**Figures S4 & S21**). For this reason, we ignored the sharp signals observed in the spectrum around 3.22 T in our simulations.

The increase in frequency from X-band to W-band can also influence which EPR transitions are allowed, which affect the intensity of these transitions. This is best observed by breaking down the contributions of the different transitions within the m_s manifolds (**Figure S5).** Using the Easyspin toolbox, we have tentatively assigned the m_s sublevel transitions at both X- and W-band; however, we note that without additional temperature and τ dependent studies, definitive assignment is not possible. At W-band, the simulated signal corresponding to the transition from the m_s = -3/2 $\rightarrow$ m_s = -1/2 manifold has an intense resonance at ~ 5 T and also corresponds to the signal observed at g_{eff} = 5.6. While we were experimentally limited to a maximum B_o of 4.5 T, it does not appear that we have a significant rising edge on the high field side of our spectrum. However, as we are extremely limited by τ (T_2 ~ 80 ns) (**Figure S2**) we believe either this transition is not observed, or the intensity is greatly diminished at W-band and our signal intensity centered at g_{eff} = 5.6 comes from the m_s = +3/2 $\rightarrow$ m_s = +1/2 transition instead. Interestingly the signal from this transition is absent at X-band frequencies, due to the relative magnitude of the microwave energy to the zero field splitting, D. Lastly, the rest of the spectrum (g_{eff} ~ 5.0, 3.0, 1.8) appears to arise from the transition from the m_s = -1/2 $\rightarrow$ m_s = +1/2 spin levels. These differences in positions and intensities highlight the importance that the spin Hamiltonian parameters modelled in W-band also fit the X-band data well.

We found that the resonant positions of the g_{eff} = 5.6, 5.0 in the X-band CW EPR spectrum were sufficiently sharp to constrain |E/D| = 0.17 (**Figure S7**), which gives us a good starting point for the simulation parameters. Moreover, we found that the g_{eff} = 5.6, 5.0 positions are highly dependent on the values of g_3 and g_2 respectively in both the X- and W-band data (**Figure S6**). The position of the high field edge position in the W-band spectrum around B_o =

2.7 T is heavily influenced by the value of g_1 (**Figure S6**). Using all three of these positions allows us to best model the spectrum with g_1, g_2, g_3 = [1.92, 1.97, 1.93].

While the spectrum at X-band is very sensitive to |E/D|, the magnitude of D is harder to determine at X-band, given $D >> \Delta E_{\mu w}$. Plotting the relative ratios of the $g_{eff} = 5.6$ and $g_{eff} = 5.0$ signals as a function of temperature can be used to provide an estimate on the sign and magnitude of D, which has previously been estimated at D = -2.2 cm^{-1}.[2,3] The W-band spectrum is much more sensitive to the magnitude of D than at X-band which greatly affects the resonant positions at W-band and overall spectral breadth of the signal. Using this observation, we found the spectrum was best modelled with D = -2.495 cm^{-1} (**Figure S7**).

NiFd-CO

The NiFd-CO spectrum is significantly more difficult to interpret and model. At X-band frequencies, the sample displays two signals that are consistent with S_{tot} = ½ and S_{tot} = 3/2 species with residual unbound $NiFd_{red}$ (**Figure S18**). Previous temperature dependent data suggest that the two signals arise from a single species with a ground spin state S_{tot} = ½ (g_1, g_2, g_3 = 2.05, 1.99, 1.90) and low-lying excited state S_{tot} = 3/2 (g_{iso} = 2.0, |E/D| = 0.05), however the exact nature and origin of these spin sublevels was not determined.[3,4] The W-band EDFS spectrum is distinctly different from the X-band spectrum, with the signal intensity collapsing to magnetic fields surrounding g ~ 2. Nutation experiments were performed to understand the relaxation behavior at different positions. The traces suggest that there may be two contributing spin states with a high frequency nutation (ν_{nut} ~40 MHz) and low frequency nutation (ν_{nut} ~10 MHz, **Figures S20 & S21**). While T_1 and T_2 relaxation rates can be correlated with spin state, the observed T_1 = 129 µs and T_2 = 251 ns values are significantly slower than the S =3/2 $NiFd_{red}$ which is in line with the expected S = ½ ground spin state. The narrowness of the W-band spectrum affords assignment of the g-tensor and ZFS tensors of the S_{tot} = ½ and S_{tot} = 3/2 states. Moreover, this provides an opportunity to understand the spin coupling model that gives rise to both the S_{tot} = ½ and S_{tot} = 3/2 states. In particular, the S = ½ state is of particular interest, as there is no conventional spin-coupling model for a cubane iron sulfur cluster that results in a S_{tot} = ½ state with a formal Ni^+, Fe^{2+}, and 2 x Fe^{3+} metal center. One distinct feature of the S = 1/2 signal is the uniquely broad and temperature dependent g_2/g_3 lineshapes at X-band and fast relaxing nature of the signal from T = 5.5 – 20 K (**Figure S1**). The unique behavior is best compared to the oxidized S_{tot} = 1/2 $[Fe_3S_4]^+$ Fd, which is known to exhibit spin canting.[5–7] In the $[Fe_3S_4]^+$ cluster, the spins of three HS Fe^{3+} centers align in a non-orthogonal manner to assume a ground spin state of S_{tot} = ½. Given the similarities of the temperature-dependent EPR spectra, we suggest that the $[Fe_3S_4]^0$ subcluster exhibits spin canting resulting in a subcluster spin, S_{Fe3} = 1. We then assume the subcluster is antiferromagnetically coupled to the single Ni^+ center to produce a ground spin state of S_{tot} = ½ and an excited state of S_{tot} = 3/2.

The NiFd-CO spectrum is then a result of the projected spin Hamiltonian parameters for $[NiFe_3S_4]^+$-CO as a result of the interaction between the intrinsic values for the Ni^+ and $[Fe_3S_4]^0$ subsites. We sought to develop a model that estimated the intrinsic values of both subcenters. To do so, we set up a spin model with Ni^+ (S_{Ni} = ½, g_1, g_2, g_3 = [2.32, 2.20, 2.09]) exchange-coupled to the $[Fe_3S_4]^0$ cluster (S_{Fe3} = 1, g1, g2, g3 = [2.01, 2.04, 2.06], |E/D| = 0.052, D = 0.84 cm^{-1}). We consider these intrinsic g-values for Ni^+ to be reasonable, considering the d^9 configuration and prior literature on Ni+ species, and expect the g-values of the $[Fe_3S_4]^0$ cluster to deviate little from g = 2 given the near-half-filled d-shells of all the iron centers. The strength and sign of the

exchange coupling, J, dictate the ground spin state, with J < 0 (AF coupling) producing a S_{tot} = ½ ground state, and magnitude of the energy spacing between the ground and excited state (**Figures S8 & S9**). The rationale used for our determination of this value will be described later.

The intrinsic g-tensors for the Ni^+ and $[Fe_3S_4]^0$ centers affect the X-/W-band simulations in different ways. A decrease in the g-tensors (g_1, g_2, g_3) of the $[Fe_3S_4]^0$ center induces a shift to lower g in the S = ½ component and a narrowing of the peak-to-peak separation in the S = 3/2 component (**Figure S14**). On the other hand, a decrease in the g-tensors for Ni^+ induces a smaller shift to higher g in the S = ½ component and a large shift to lower magnetic field for the S = 3/2 component (**Figure S14**). This differential shift and final projected g-tensors (for S =1/2, g_{iso} < 2) highlight that the spin projection is higher on the Fe centers than the Ni center, which has previously been observed in other heterometallic clusters and to be expected given the electronic configuration of the different metals.[8,9] Additionally, the sharp feature that we preliminarily assign as the S = 3/2, m_s = -1/2 → m_s = -3/2 transition at B_0 ~ 3.25 T (**Figure S13**, ν = 94 GHz) was used to refine the g-tensors of the Ni^+ and $[Fe_3S_4]^0$ cluster in conjunction with the g = 2.05 and 1.99 features around B_0 ~ 3.3 – 3.4 T (ν = 94 GHz). Visualization of the pseudo-modulated spectra assisted in refining resonant positions for the simulation (**Figure S10**). These values were iteratively modified to find the best fit to the data resulting in intrinsic values of S_{Ni} = ½; g_1, g_2, g_3 = [2.32, 2.20, 2.09] and S_{Fe3} = 1; g_1, g_2, g_3 = [2.01, 2.04, 2.06], which result in projected values of S = ½; g_1, g_2, g_3 = [1.91, 1.99, 2.05] and S = 3/2; g_1, g_2, g_3 = [2.12, 2.09, 2.07]. Due to the broad lineshape of the g_1 transition, it is difficult to assign this value accurately. Similar resolution issues have been observed at X- and Q-band for the spin-canted $[Fe_3S_4]^+$ cluster. The intrinsic g_1 values did affect the position of the S = 3/2 signal and g_1 transition in X-band, so we were able to determine that this value is a good fit for the ZFS obtained.

As the Ni^+ center exhibits a spin S_{Ni} = ½, the ZFS of the $[Fe_3S_4]^0$ subcluster dominates the projected values of the S = 3/2 component. We found that the signals corresponding to g_{eff} = 4.3 and 3.8 were highly sensitive to small changes in |E/D| in the X-band spectrum (**Figure S15**). However, the W-band spectrum was nearly insensitive to the same changes in |E/D|. For this reason, we were able to use the X-band spectrum to constrain the rhombicity of the ZFS for the $[Fe_SS_4]^0$ subcluster to |E/D| = 0.052. The magnitude of D influences the positions in W-band and X-band to a great degree (**Figure S16**). It appears that the magnitude of D affects the spectral breadth at W-band, with larger values moving the position of the broad shoulder on the low field side to lower fields, corresponding to the transition from the m_s = -1/2 → m_s = +1/2 sublevels. Likewise, in the X-band spectrum, increasing D shifts the S = 3/2 signal to lower field. However, a much more drastic shift to higher fields is observed upon lowering the zero-field splitting at X-band, which allowed us to constrain the intrinsic D for the $[Fe_3S_4]^0$ subcluster to D = +0.84 cm^{-1}, resulting in a projected D-tensor, D_1, D_2, D_3 = [-2361, -3234, 5596 MHz].

Once the positions and spectra were well reproduced, it was possible to use these values to model the exchange coupling of the Ni^+ and $[Fe_3S_4]^0$ centers. As mentioned above, the magnitude of J dictates the energy difference between the S = 1/2 ground state and S = 3/2 excited state, with the populations of each given by the Boltzmann distribution. Given that we observe both the ground and excited states at low temperatures (T = 4 K), we believed that our exchange coupling between these two centers must be weak, J < 10 cm^{-1} (**Table S1, Figures S11 & S12**). In order to estimate the exchange coupling, we fit variable temperature spectra of a NiFd-CO sample from 4 – 15 K to determine the weighted contributions of the S = 3/2 and S = ½ states (**Table S2, Figures S17 & S18**). It is worth noting that the lineshape of the spin-canted S = ½ signal is difficult to recreate, leading to an imperfect overlap in the simulation. This is

evident in the sharp feature observed in the residual traces, which is an artifact of the subtraction (**Figure S18**). However, the intensities of the g = 2.05 and 1.99 features are still viable to fit the relative intensities and population of the S = ½ and S =3/2 states. The experimentally determined values from the variable temperature X-band CW spectral fits most closely align with J = -1.0 cm^{-1} (**Figure S17**). The populations expected at 5 K do not perfectly match those observed in the W-band EDFS; however, we believe that the relative intensities of the EDFS spectrum may be affected by differential relaxation at the different field positions (similar to the $NiFd_{red}$), and therefore we believe the CW X-band EPR spectra more accurately reflect the populations of the S =1/2 and S = 3/2 states.

While we acknowledge that the simulations for the multifrequency data are not perfect, it is important to note that (i) these are the first reported ESE-EPR spectra of high-spin biological clusters on the W-band HiPER instrument and establish precedent for the method to be applied not only to our model cluster but other rapidly relaxing species and even the native enzyme and (ii) the multifrequency spectra appropriately constrain the major spin Hamiltonian parameters (g, D, and |E/D|). We do acknowledge that the parameters determined from the simulations are not exact nor unique, but they do give insight into the asymmetry of the cluster through the g- and D-tensors. Additionally, the distinctions between $NiFd_{red}$ and NiFd-CO suggest a complete change in the exchange interactions across the cluster from a fully integrated, strongly exchange coupled system to a weakly exchange coupled system that isolates spin and electron density to the Ni-CO subsite, which we hypothesize isolates reactivity to that site as well. Moreover, the EPR simulations are in good agreement with the spin Hamiltonian parameters obtained using Mössbauer spectroscopy. By coupling the information obtained from both techniques, we are able to understand the perturbations to both the cluster as a whole and the iron sites upon binding of CO to $NiFd_{red}$.

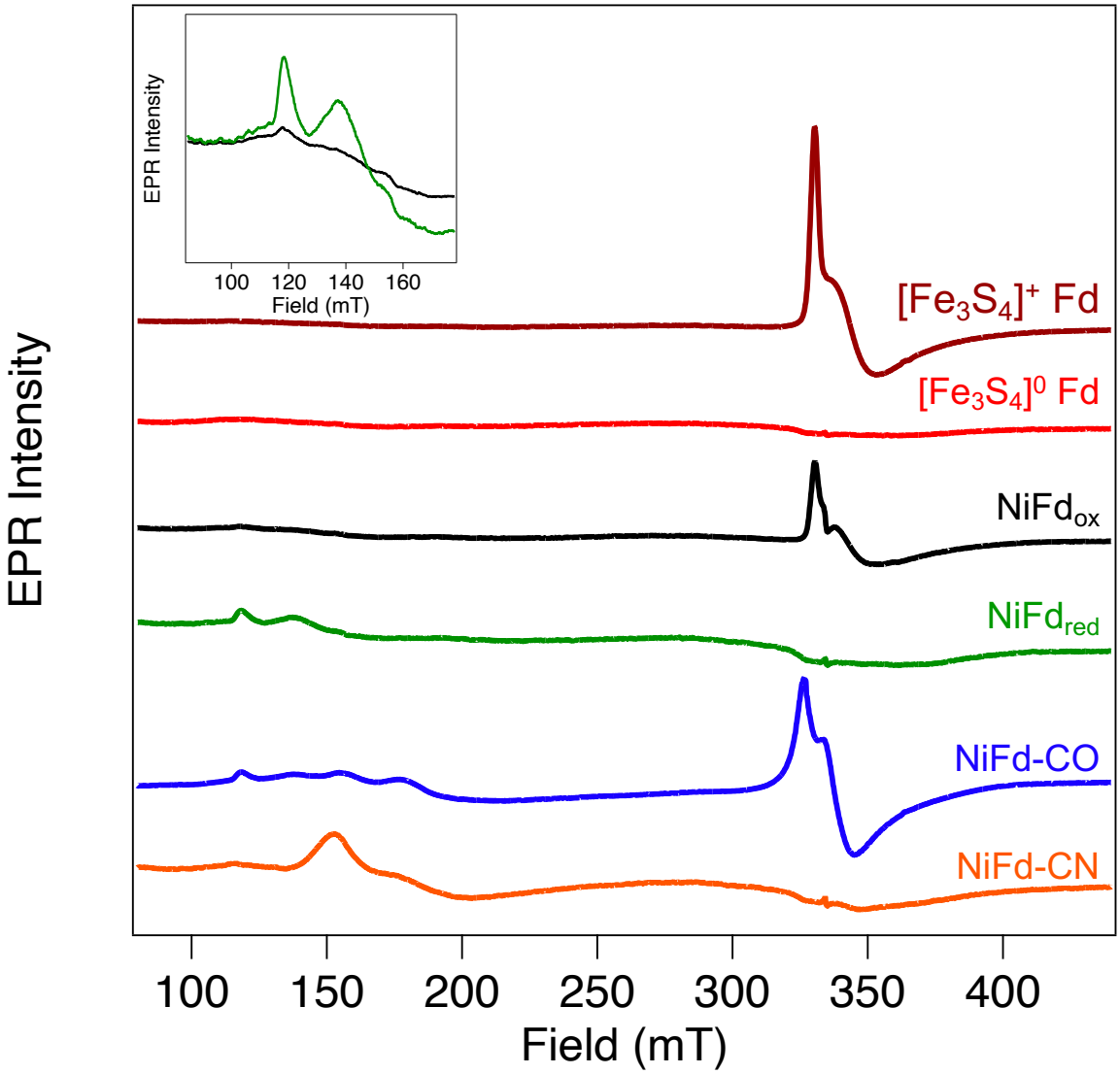

Figure S22. CW EPR spectra (ν = 9.37 GHz, T = 8 K, $P_{\mu w}$ = 20 mW) of $[Fe_3S_4]^+$ Fd (brown), $[Fe_3S_4]^0$ Fd (red), $NiFd_{ox}$ (black), $NiFd_{red}$ (green) NiFd-CO (blue), NiFd-CN (orange). (**Inset**) Overlay of $NiFd_{red}$ and $NiFd_{ox}$ indicative of incomplete oxidation by thionine.

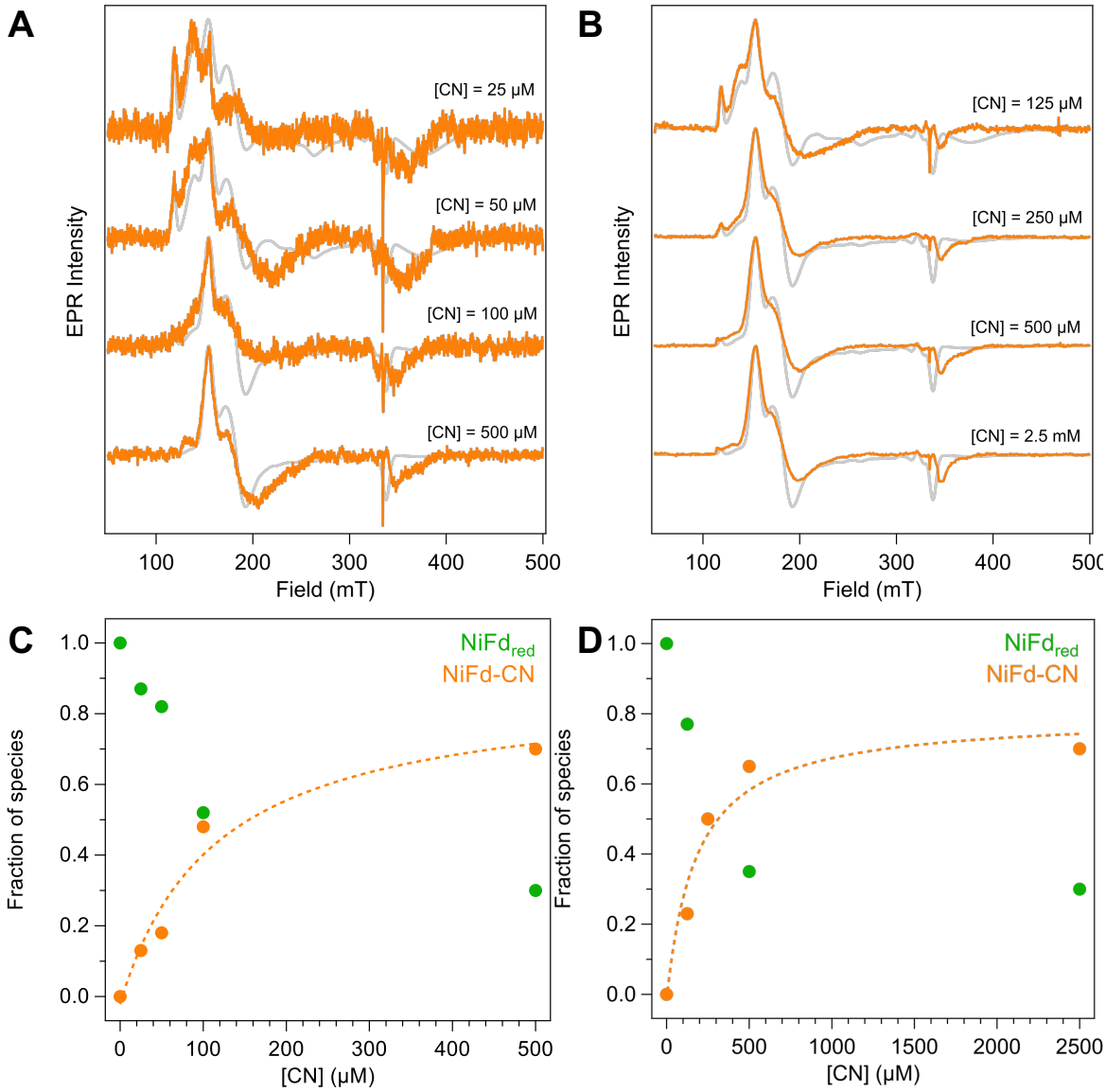

Figure S23. X-band CW-EPR spectra for (**A**) 50 µM NiFd and (**B**) 250 µM NiFd at varying CN^- concentrations with spectra shown in orange and simulations in grey. (**C**)- (**D**) Binding curves for CN^- binding to NiFd based on EPR spectra. The fraction of NiFd-CN and $NiFd_{red}$ present at varying CN^- concentrations was determined based on EPR spectral simulations. An approximate K_D of ~ 160 µM was calculated by fitting the data sets at (**C**) 50 µM and (**D**) 250 µM $NiFd_{red}$ to the Langmuir binding equation based on a one-site binding model. For the individual concentrations, at 50 µM NiFd, the calculated K_D was 114.03 ± 61.9 µM and at 250 µM, the calculated K_D was 179.19 ± 93.4, showing good convergence between the two data sets.

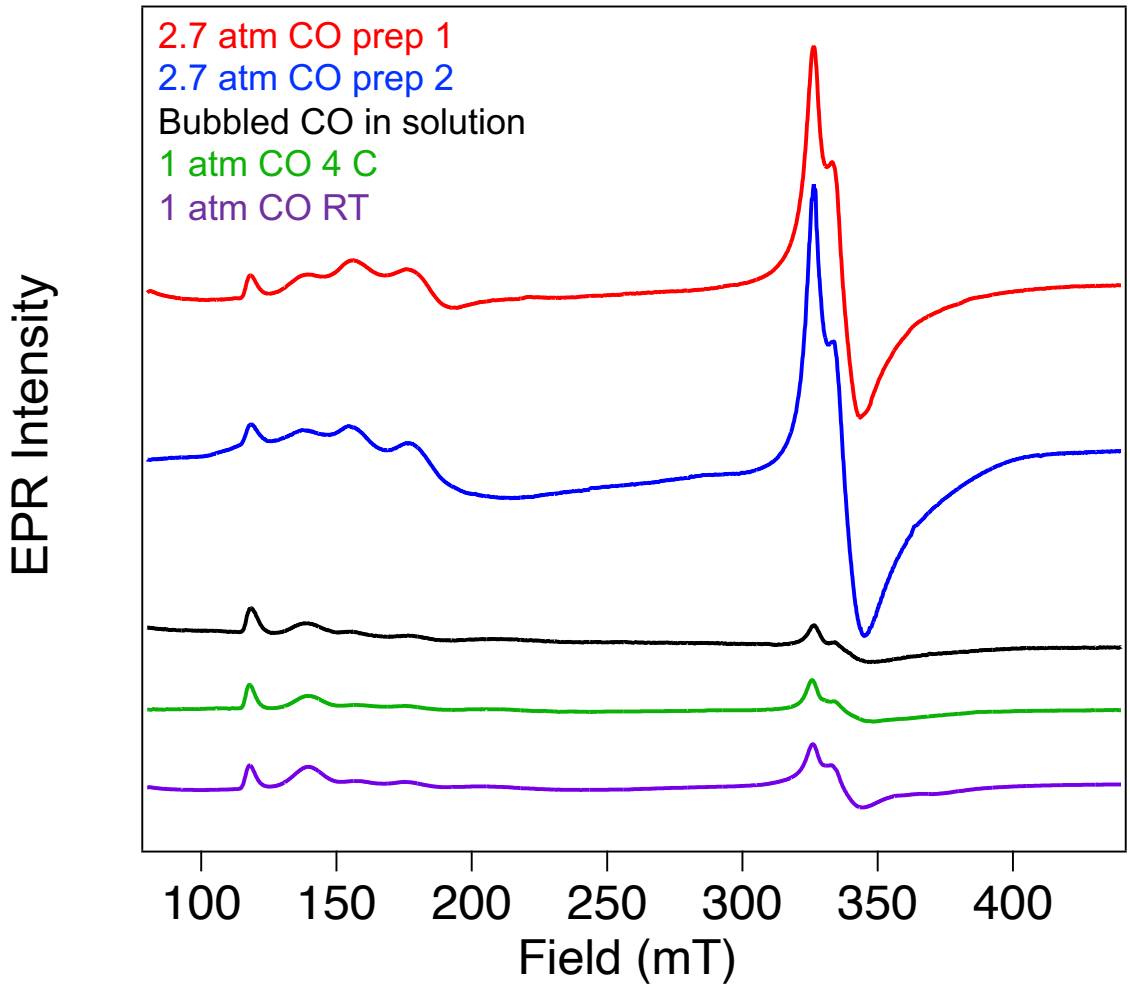

Figure S24. CW EPR spectra (ν = 9.37 GHz, T = 8 K, $P_{\mu W}$ = 20 mW) of NiFd-CO using different preparation methods. Binding of CO is optimal and reproducible upon pressurization of the headspace of $NiFd_{red}$ with CO at 2.7 atm at RT.

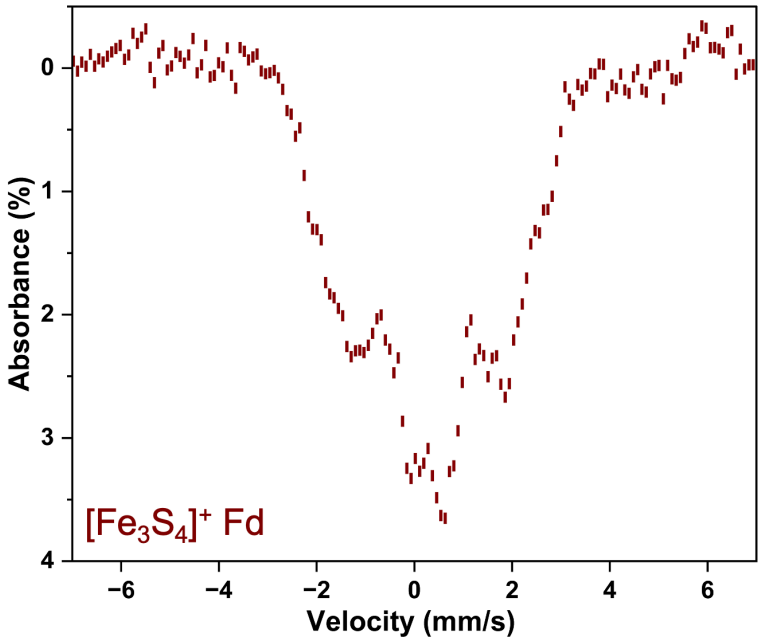

Figure S25. 4.2 K Mössbauer spectra (raw data) collected in a parallel applied magnetic field of 1 kG for $[Fe_3S_4]^+$ Fd.

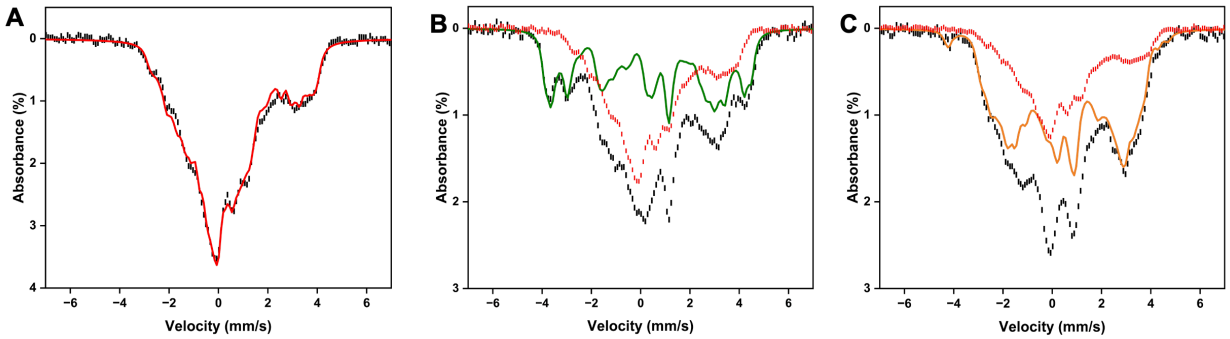

Figure S26. 4.2 K Mössbauer spectra (raw data) collected in parallel applied magnetic fields of 1 kG for (A) $[Fe_3S_4]^0$, (B) $NiFd_{red}$, and (C) NiFd-CN. Raw data are shown as black hash mark curves. The $[Fe_3S_4]^0$ sample was pure as judged from the variable field data collected and simulation of the data using previously reported parameters from Srivastava et al.[10] Spectra shown in panels (B) and (C) show that the reduced heterometallic cluster as well as its cyanide bound state (NiFd-CN) contain contributions from 50% and 35% $[Fe_3S_4]^0$ (red), respectively. The green and orange curves in (B) and (C) represent the desired species for each.

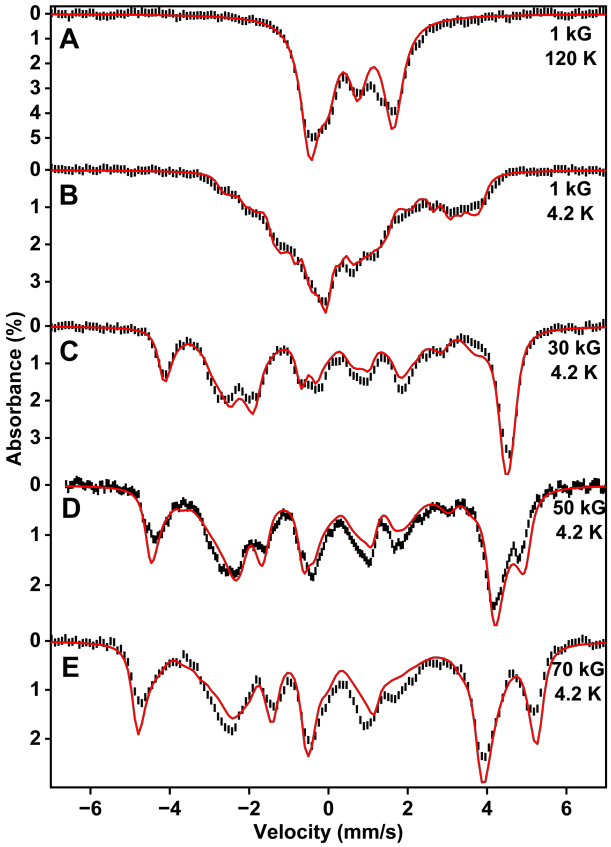

Figure S27. Mössbauer spectra of $[Fe_3S_4]^0$ ferredoxin collected in parallel applied magnetic fields from 1–70 kG. Experimental spectra (black hash-mark lines) are overlaid with simulations (red solid lines). The good agreement between the experimental and simulated spectra demonstrate convergence between the spectral assignments and experimental data. The simulations are prepared using the parameters listed in Table 1. The spectrum in panel A was recorded at 120 K, whereas spectra in panels B-E were recorded at 4.2 K.

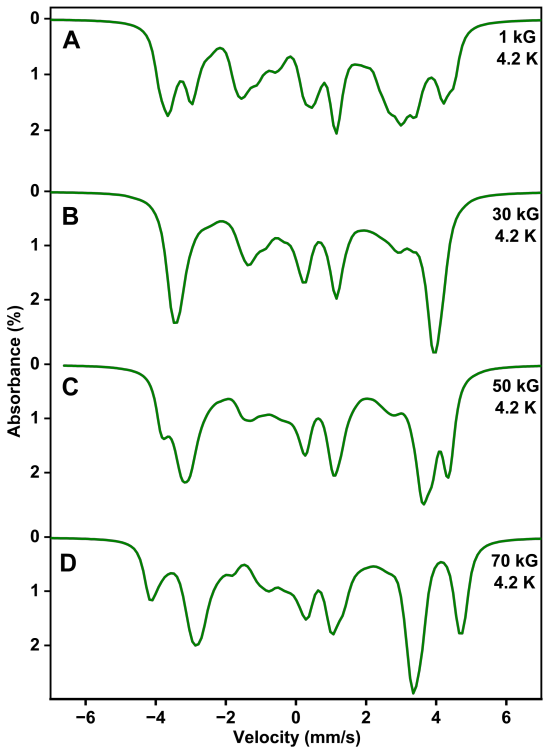

Figure S28. Simulations for 4.2 K, variable-field (1–70 kG) Mössbauer spectra (green) for $NiFd_{red}$. Simulations were generated using the parameters from Table 1. The simulated spectra were used to subtract $[NiFe_3S_4]^+$ contributions from the $NiFd_{ox}$ and NiFd–CO spectra (Figures S29 and S30).

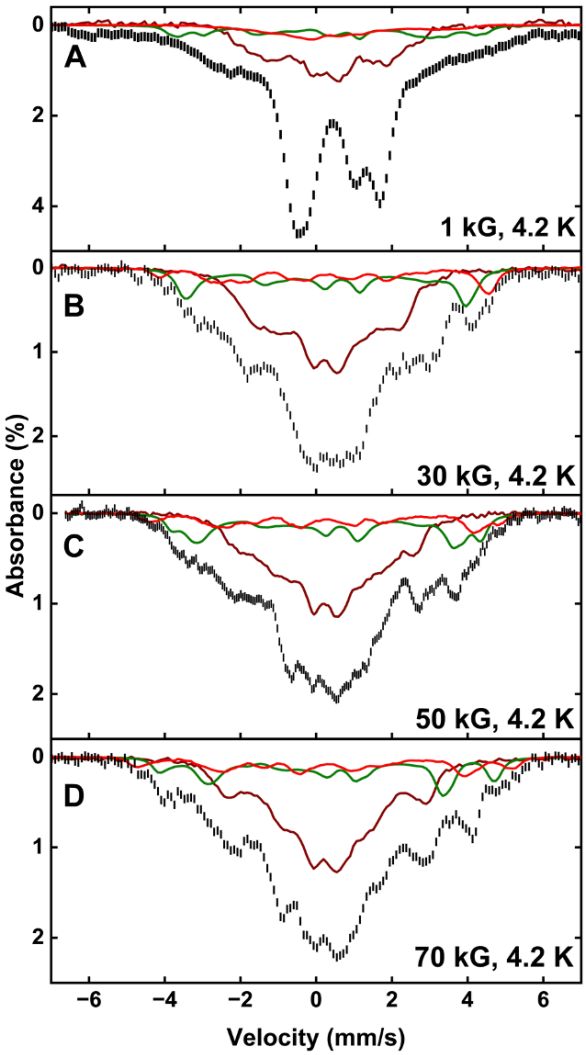

Figure S29. Mössbauer spectra of $NiFd_{ox}$ collected at 4.2 K collected in increasing applied magnetic fields of (A) 1 kG, (B) 30 kG, (C) 50 kG, and (D) 70 kG. Raw experimental data are shown in black. The fits include contributions from ~34% experimental $[Fe_3S_4]^+$ Fd (brown), ~15% simulated $NiFd_{red}$ (green), and ~9% experimental $[Fe_3S_4]^0$ (red).

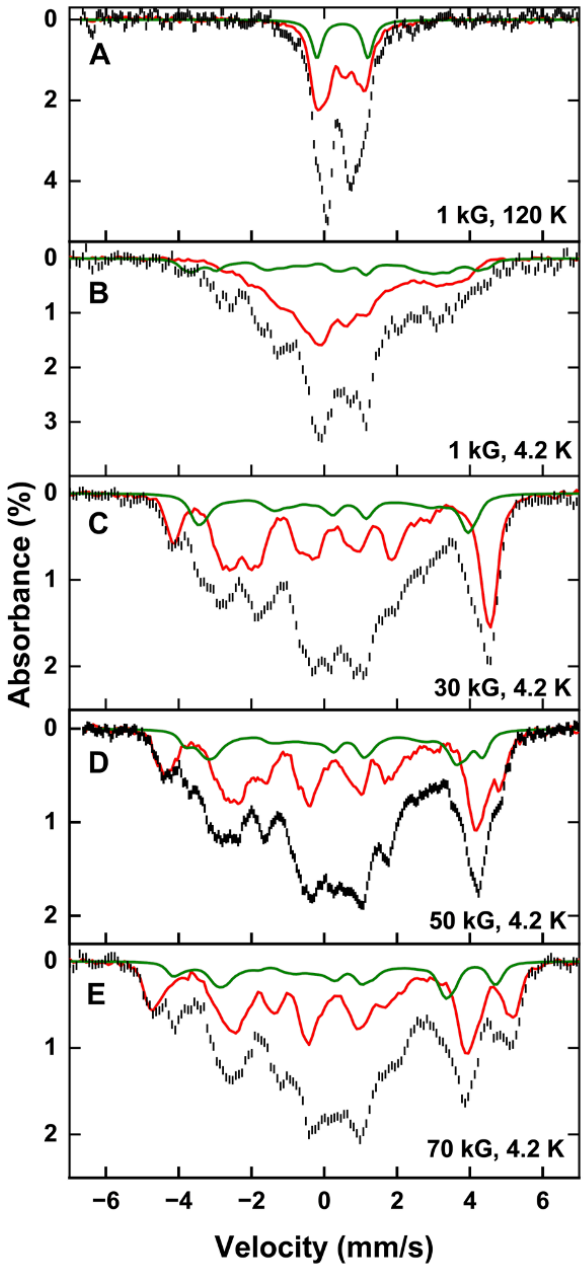

Figure S30. Variable field Mössbauer spectra of NiFd-CO collected at 4.2K. The black hash mark curves are the raw experimental data. The red curves are experimental spectra of pure $[Fe_3S_4]^0$ recorded at each field shown at 45% intensity. The green curves are simulations of $NiFd_{red}$ shown at 15% intensity. The red and green traces were subsequently removed, leaving ~40% of the total sample and >70% of the NiFd sample that can be attributed to the CO-bound species. The difference spectra are shown in **Figure 5** of the main text, and are taken to be the spectra of pure NiFd-CO.

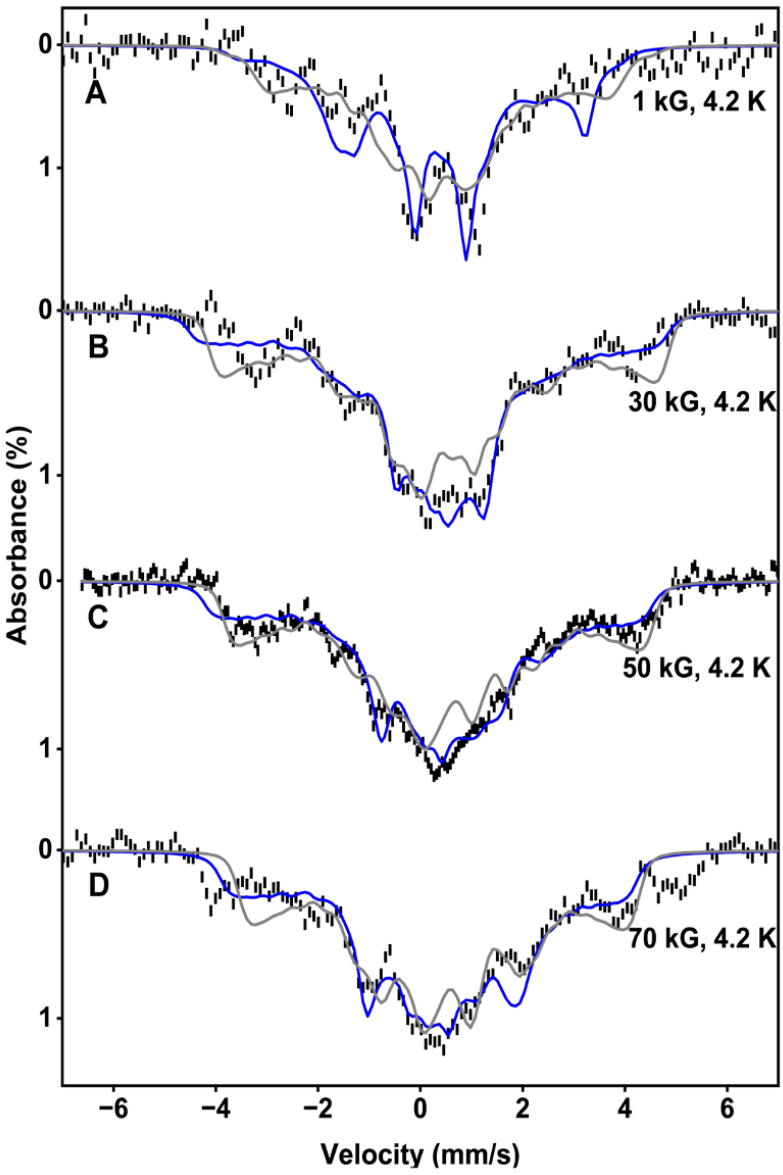

Figure S31. Mössbauer spectra of NiFd-CO collected at 4.2 K in parallel applied magnetic fields of (A) 1kG, (B) 30 kG, (C) 50 kG, and (D) 70 kG. The black hash marked spectra represent the difference spectra, corresponding to 40% NiFd-CO, obtained after subtraction of 45% $[Fe_3S_4]^0$ (experimental data) and ~15% $NiFd_{red}$ (simulation). The blue curves are simulations of the experimental difference spectra using the two-site model shown in **Figure 5**. The gray curves are representative simulations of NiFd-CO if the system had a well isolated ground spin state of S = ½.

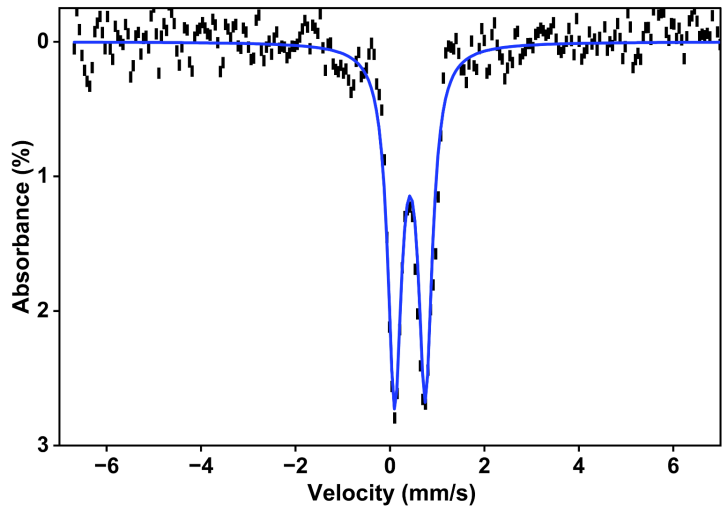

Figure S32. Mössbauer spectrum of NiFd-CO collected at 120 K in a parallel applied magnetic field of 1kG. The black hash marked spectrum represents the difference spectrum, corresponding to 40% NiFd-CO, obtained after subtraction of 45% $[Fe_3S_4]^0$ (experimental data) and ~15% $NiFd_{red}$ (simulation). The blue curves are simulations of the experimental difference spectra used to constrain the isomer shift, δ = 0.45 mm/s and ΔE_Q = 1.2 mm/s.

Discussion of $[Fe_3S_4]^+$ Fd, $[Fe_3S_4]^0$ Fd, $NiFd_{red}$, $NiFd_{ox}$, NiFd-CN, and NiFd-CO Mössbauer spectra

The 4.2 K, 1 kG Mössbauer spectrum of $[Fe_3S_4]^+$ Fd closely resembles that previously reported for oxidized *D. gigas* $[Fe_3S_4]^+$ Fd II (**Figure S25**), with broad spectral features arising from three high-spin ferric centers (δ = 0.27 mm/s, ΔE_Q = 0.54 mm/s; Table 1). Although the three iron sites share identical δ and ΔE_Q values, distinct hyperfine parameters are observed, consistent with prior analyses by Münck and coworkers.[11] The spin-coupling scheme produces an overall S_{tot} = 1/2 ground state that is best described as having two ferric sites that form an intermediate spin manifold ($S' = 2$ or 3) being antiferromagnetically coupled to a third S = 5/2 ferric site.[5,11]

Reduction of $[Fe_3S_4]^+$ Fd to $[Fe_3S_4]^0$ yields two mixed-valent $Fe^{2.5+}$sites (δ = 0.47 mm/s, ΔE_Q = 1.47 mm/s) and one ferric site (δ = 0.31 mm/s, ΔE_Q = 0.50 mm/s), in agreement with previous reports (**Figures S26A and S27).**[5,10,12] The hyperfine parameters support formation of a double-exchange-coupled $Fe^{2.5+}$– $Fe^{2.5+}$ dimer ($S' = 9/2$) that is antiferromagnetically coupled to a ferric S = 5/2 site, yielding a system with total spin, S_{tot} = 2.

The experimental data collected for $[NiFe_3S_4]^+$ ($NiFd_{red}$) revealed that the sample contained 50% of the desired species and 50% of the reduced three-iron cluster ($[Fe_3S_4]^0$), suggestive of non-quantitative metalation with Ni (**Fig. S26B**). The species was fit assuming a total spin of S=3/2. Simulation of low temperature data collected in variable applied magnetic fields revealed that the three iron sites displayed distinct magnetization behaviors. Two of the sites were fit using negative hyperfine values, reminiscent of the delocalized iron sites in the reduced $[Fe_3S_4]$ cluster, and one site was fit with positive hyperfine values.

Oxidation of $NiFd_{red}$ yields $NiFd_{ox}$, which contains multiple species due to partial oxidation. Mössbauer analysis indicates that the sample consists of ~42% $NiFd_{ox}$, ~15% $NiFd_{red}$, ~34% $[Fe_3S_4]^+$ Fd, and ~9% $[Fe_3S_4]^0$ Fd (**Figure S29**). In comparison to the $NiFd_{red}$ sample, there is no significant increase in total $[Fe_3S_4]$ Fd species (50% in $NiFd_{red}$ vs 43% in $NiFd_{ox}$) highlighting the stability of the NiFd species upon oxidation. $NiFd_{ox}$ exhibits a $S_{tot} = 1$ ground state (E/D = 0.22, D = −1.9 cm^{-1}), with two equivalent mixed-valent $Fe^{2.5+}$ sites antiferromagnetically coupled to a ferric Fe^{3+} site. Hyperfine anisotropy differences suggest distinct ligand-field environments for Fe_3 relative to Fe_1 and Fe_2.

The Mössbauer spectra of NiFd-CN revealed that the sample contained 65% of the NiFd-cyanide bound species (**Fig. S26C**, orange), with the remaining 35% accounted for by the $[Fe_3S_4]^0$ cluster, highlighting quantitative binding of CN^- to $NiFd_{red}$. The spectra of the cyanide-bound species could be fit assuming a total spin of the system is S=3/2. The parameters used to simulate the CN-bound state are consistent with those previously reported by Srivastava et al.[10]

In summary, these data confirm that the nickel-deficient as well as the nickel-loaded enzymes can be simulated (and described) using the same or similar parameters as reported in previous work.[13,14] These spectra serve as spectroscopic benchmarks from which to calibrate our studies of the oxidized heterometallic cluster as well as the CO-bound CODH mimic.

Binding of CO to $NiFd_{red}$ yields NiFd–CO which has a $S_{tot} = 1/2$ ground state and a low-lying S = 3/2 excited state that is appreciably populated at 4.2 K. Simulation of the CO-bound species were performed on difference spectra obtained by subtracting contributions from ~ 45% $[Fe_3S_4]^0$ and 15% $NiFd_{red}$ (**Figure S30**), corresponding to ~70% binding of CO to $NiFd_{red}$ under these conditions. Because of the nature of NiFd-CO, we had to adopt a different approach to fitting the experimental Mössbauer data compared to the approach used to fit data for the other species tabulated in Table 1. The Hamiltonian used to simulate the NiFd-CO spectra has several terms. The first consists of the zero-field splitting contribution from the iron cluster and the electronic Zeeman term for the iron cluster:

$$\mathcal{H}_c = D\left(S_{z,c}^2 - \frac{2}{3}\right) + E\left(S_{x,c}^2 - S_{y,c}^2\right) + \beta \boldsymbol{S}_c \cdot \boldsymbol{g}^c \cdot \boldsymbol{H} \quad \textbf{(1)}$$

The second includes the electronic Zeeman term for the Ni-CO moiety:

$$\mathcal{H}_{Ni-CO} = \beta \boldsymbol{S}_{Ni-CO} \cdot \boldsymbol{g}^{Ni-CO} \cdot \boldsymbol{H} \quad \textbf{(2)}$$

Finally, the exchange interaction term that describes the coupling between the Fe cluster and the Ni-CO moiety can be written as:

$$\mathcal{H}_{exchange} = j\boldsymbol{S_c} \cdot \boldsymbol{S}_{Ni-CO} \quad \textbf{(3)}$$

The j term couples the Fe-S cluster to the Ni^+-CO site.

However, because ^{57}Fe Mössbauer spectroscopy is “Ni silent”, in the two-spin framework, the contributions to the Mössbauer simulation sites come exclusively from the irons in the cluster. The parameters provided in Table 1 of the main text were obtained in the context of the Hamiltonian above, and included contributions from the magnetic hyperfine, nuclear magnetic moment, and quadrupole interactions.

$$\mathcal{H} = \sum_i \left[\left(S \cdot \vec{\boldsymbol{A}}_i \cdot \boldsymbol{I}_i\right) + \left(\boldsymbol{g}_n \beta_n \boldsymbol{H} \cdot \boldsymbol{I}_i\right) + \mathcal{H}_Q\right] \quad \textbf{(4)}$$

The simulation parameters for the CO-bound species are reported with the understanding that they may not represent a unique solution due to the limitations of the parameterization space the data are analyzed in. Additionally, as noted in the main text, we use the high temperature spectrum to justify simulation of the iron sites in the cluster using the average of their parameters (treating them as identical). Considering only isotropic Zeeman and exchange interactions allows us to work with more tractable matrices that can be used to derive the energy level diagrams for the NiFd-CO species and to fit our spectroscopic data.

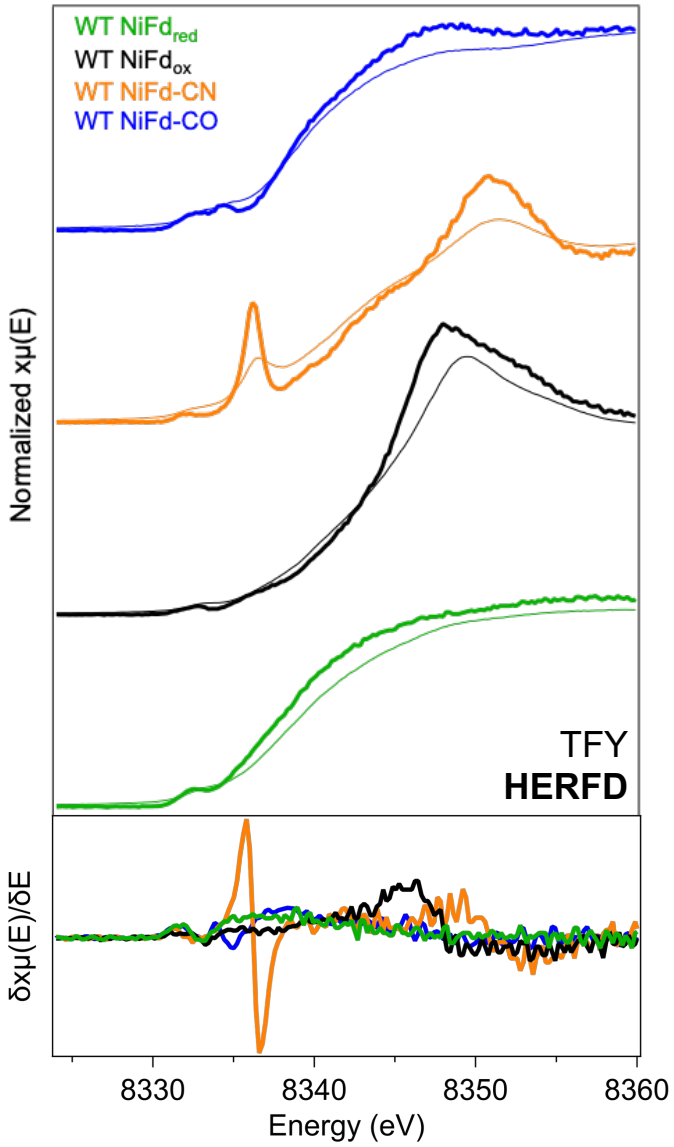

Figure S33. Ni Kα XAS of NiFd samples (as indicated) comparing the signal and spectral resolution of total fluorescence yield-detected (TFY; thin lines) with high energy resolved fluorescence-detected (HERFD; thick lines) spectra (*top*). The representative first derivatives of the spectra shown in the top panel (*bottom*).

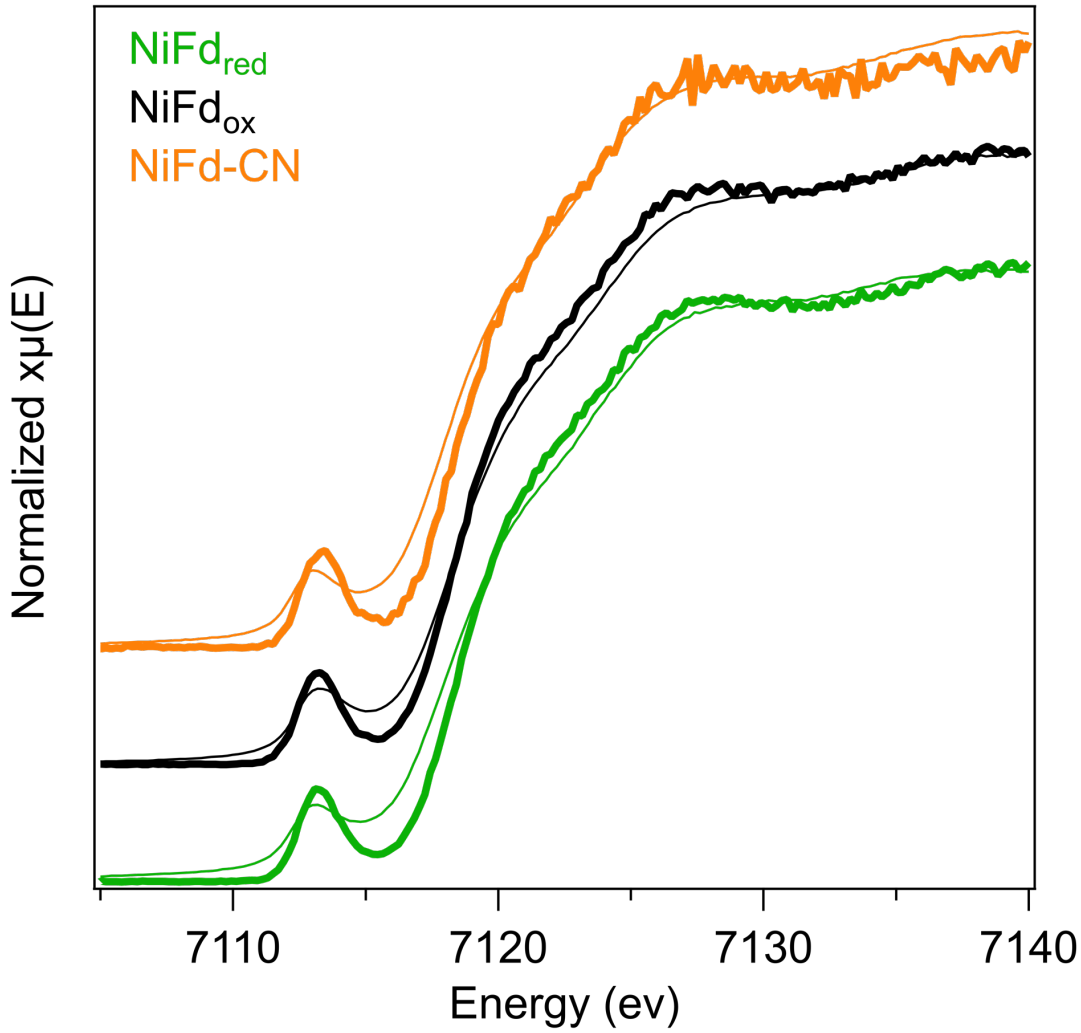

Figure S34. Fe Kα XAS of NiFd samples (as indicated) comparing the signal and spectral resolution of total fluorescence yield-detected (TFY; thin lines) with high energy resolved fluorescence-detected (HERFD; thick lines) spectra.

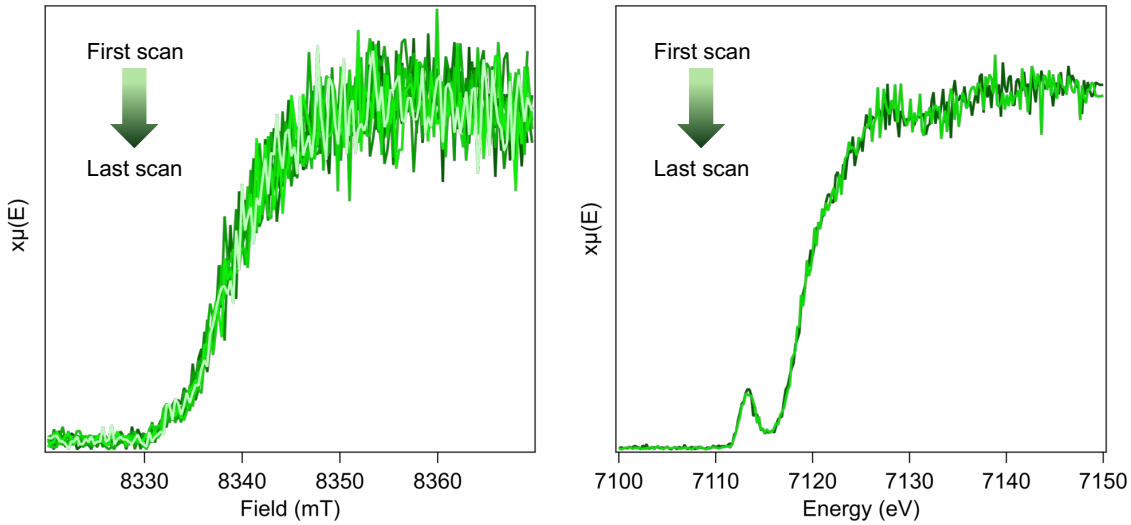

Figure S35. Ni (left) and Fe (right) Kα HERFD XANES photodamage test scans for $NiFd_{red}$. A total of 8 successive scans were completed on the same sample position equaling 480 seconds of radiation exposure for Ni HERFD XANES and a total of 2 scans equaling 860 seconds of radiation exposure were completed for Fe HERFD XANES.

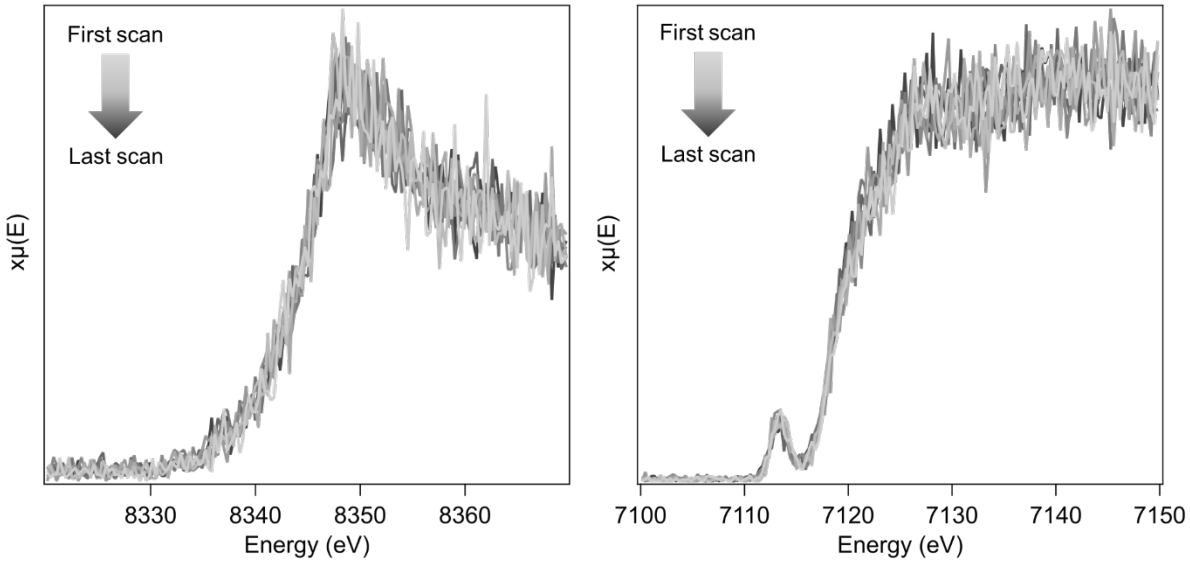

Figure S36. Ni (left) and Fe (right) Kα HERFD XANES photodamage test scans for $NiFd_{ox}$. A total of 8 successive scans were completed on the same sample position equaling 480 seconds of radiation exposure for both Ni and Fe HERFD XANES.

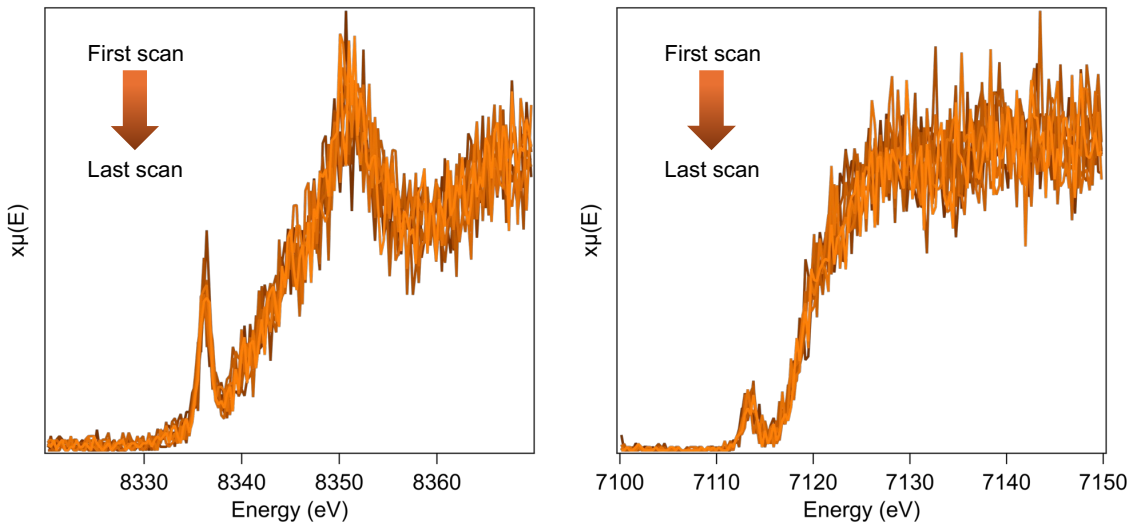

Figure S37. Ni (left) and Fe (right) Kα HERFD XANES photodamage test scans for NiFd-CN. A total of 8 successive scans were completed on the same sample position equaling 480 seconds of radiation exposure for both Ni and Fe HERFD XANES.

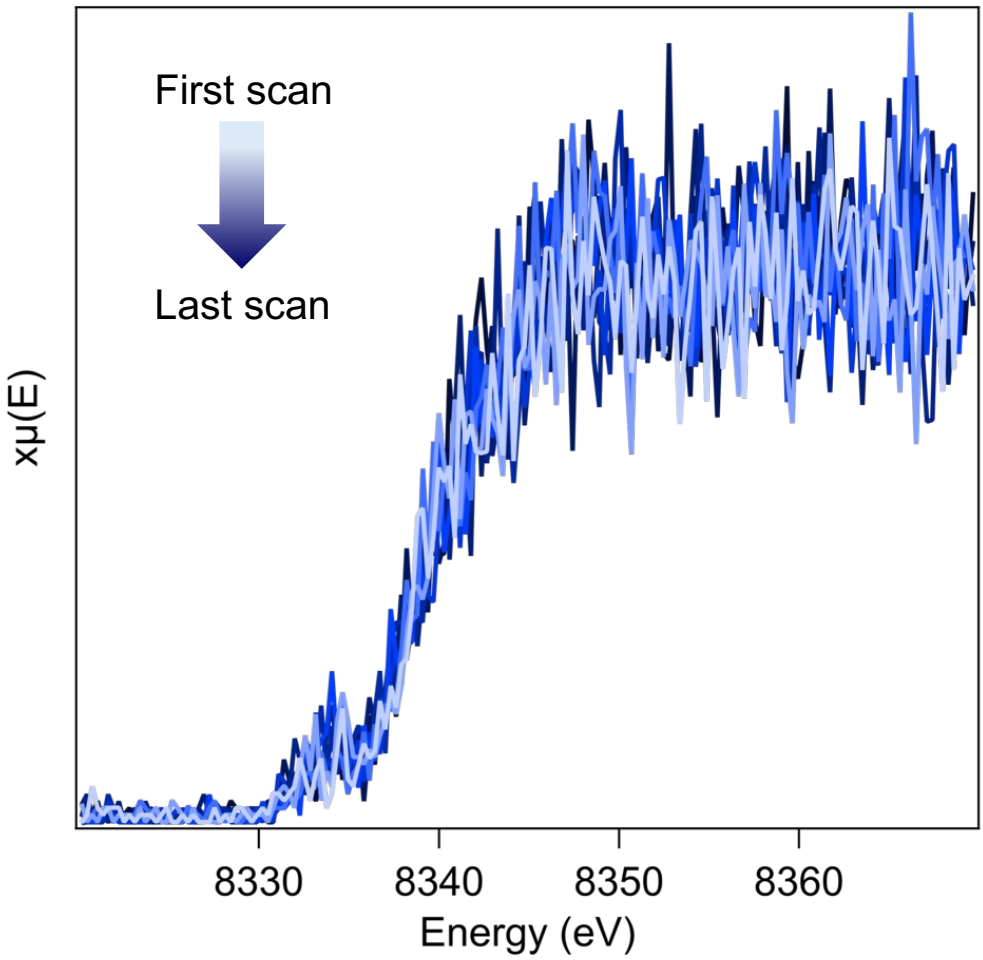

Figure S38. Ni (left) Kα HERFD XANES photodamage test scans for NiFd-CO. A total of 10 successive scans were completed on the same sample position equaling 600 seconds of radiation exposure for Ni HERFD XANES.

Sample	Pre-edge Position(s) / eV	Edge Position / eV
$NiFd_{ox}$	8331.5, 8332.8	8342.3
$NiFd_{red}$	8332.7	8338.4
NiFd-CN	8332.1, 8336.2	8342.3
NiFd-CO	8334.4	8339.3

Table S3. Pre-edge and edge energies for samples from Ni Kα HERFD-XAS measurements. Edge positions were taken as the energy at which the intensity reached half the value of the normalized intensity.

Sample	Pre-edge Position / eV	Edge Position / eV
$NiFd_{ox}$	7113.5	7119.2
$NiFd_{red}$	7113.3	7119.4
NiFd-CN	7113.1	7119.4

Table S4. Pre-edge and edge energies for samples from Fe Kα HERFD-XAS measurements. Edge positions were taken as the energy at which the intensity reached half the value of the normalized intensity.

	Energies (kcal/mol)			NPA Charges												Spin Density											
State	QM, PC	QM, no PC	big-QM, PC	Ni	Fe1	Fe2	Fe3	S1	S2	S3	S4	Cys1 S	Cys2 S	Cys3 S	CO/ Asp O	Ni	Fe1	Fe2	Fe3	S1	S2	S3	S4	Cys1 S	Cys2 S	Cys3 S	CO/ Asp O
NiFd-CO																											
HS	22.29	21.68	-	0.48	0.73	0.63	0.78	-0.72	-0.77	-0.69	-0.84	-0.39	-0.42	-0.47	-0.10	0.80	3.71	3.70	3.75	0.62	0.57	0.57	0.53	0.24	0.22	0.19	0.03
BS1	0	0	-	0.48	0.64	0.35	0.63	-0.50	-0.71	-0.54	-0.80	-0.30	-0.43	-0.49	-0.11	-0.68	-3.60	2.31	3.43	-0.04	-0.07	0.03	-0.25	-0.02	-0.18	0.09	-0.03
BS2	11.65	10.25	-	0.47	0.54	0.53	0.57	-0.63	-0.60	-0.56	-0.78	-0.39	-0.37	-0.45	-0.09	-0.70	2.92	-3.53	3.05	-0.25	-0.15	0.02	-0.21	-0.18	0.03	0.04	-0.03
BS3	5.47	4.29	-	0.48	0.55	0.40	0.65	-0.60	-0.72	-0.56	-0.70	-0.33	-0.39	-0.48	-0.07	-0.71	3.04	2.82	-3.61	-0.15	-0.20	0.03	-0.14	0.05	0.04	-0.15	-0.03
$NiFd_{red}$																											
HS	22.97	22.25	23.08	0.91	0.73	0.72	0.76	-0.92	-0.89	-0.82	-0.88	-0.49	-0.42	-0.59	-0.79	1.37	3.68	3.65	3.72	0.46	0.48	0.52	0.56	0.14	0.20	0.13	0.03
BS1	7.37	6.99	7.47	0.79	0.61	0.65	0.68	-0.84	-0.79	-0.72	-0.74	-0.50	-0.42	-0.58	-0.80	-0.99	-3.54	3.58	3.57	0.31	-0.05	0.15	-0.07	0.12	-0.17	0.10	-0.01
BS2	6.57	4.96	7.26	0.84	0.66	0.58	0.66	-0.84	-0.81	-0.72	-0.74	-0.49	-0.43	-0.59	-0.79	-1.14	3.59	-3.47	3.54	-0.03	0.28	0.15	-0.11	-0.10	0.18	0.11	-0.02
BS3	0	0	0	0.82	0.67	0.66	0.63	-0.82	-0.79	-0.73	-0.81	-0.50	-0.42	-0.58	-0.79	-1.09	3.58	3.55	-3.52	-0.05	-0.04	0.10	0.30	0.11	0.16	-0.10	-0.02
$NiFd_{ox}$																											
HS	33.67	32.95	-	1.09	0.78	0.76	0.78	-0.81	-0.78	-0.74	-0.78	-0.45	-0.32	-0.53	-0.81	1.59	3.83	3.76	3.74	0.54	0.59	0.56	0.62	0.19	0.23	0.15	0.05
BS1	4.08	4.76	-	1.02	0.64	0.65	0.66	-0.80	-0.66	-0.57	-0.65	-0.44	-0.32	-0.51	-0.82	-1.43	-3.65	3.57	3.53	0.28	-0.19	0.10	-0.20	0.16	-0.24	0.11	-0.03
BS2	2.74	2.20	-	1.01	0.62	0.64	0.67	-0.71	-0.72	-0.56	-0.65	-0.40	-0.37	-0.53	-0.81	-1.41	3.52	-3.65	3.55	-0.13	0.20	0.08	-0.23	-0.19	0.19	0.12	-0.04
BS3	0	0	-	1.00	0.63	0.65	0.66	-0.71	-0.66	-0.57	-0.72	-0.44	-0.35	-0.49	-0.81	-1.41	3.51	3.57	-3.64	-0.18	-0.21	0.02	0.20	0.14	0.18	-0.15	-0.04

Table S5. BS-DFT energy levels for NiFd-CO, $NiFd_{red}$, and $NiFd_{ox}$, with natural population analysis charges (indicated by "q" prefix) and Mulliken spin densities (indicated by "s" prefix).

Fe site	δ	ΔE_Q	A_{iso} (kG)
$NiFd_{red}$			
Fe1	0.36	0.72	-21.94
Fe2	0.42	1.10	-21.47
Fe3	0.36	-1.10	-23.05
NiFd-CO			
Fe1	0.31	-0.58	-22.53
Fe2	0.17	-1.11	-20.37
Fe3	0.31	0.82	-20.33
$NiFd_{ox}$			
Fe1	0.21	-1.25	-19.87
Fe2	0.29	1.54	-20.81
Fe3	0.28	1.40	-19.81

Table S6. Calculated Mossbauer parameters at optimized QM/MM geometries for the high-spin state.

State	ΔE	S_{Ni}	S_{Fe1}	S_{Fe2}	S_{Fe3}	S_{tot}
BS1	4.08	-1	-5/2	5/2	2	1
BS2	2.74	-1	2	-5/2	5/2	1
BS3	0	-1	5/2	2	-5/2	1
BS4	13.24	-1	-2	5/2	5/2	2
BS5	10.68	-1	5/2	-2	5/2	2
BS6	7.79	-1	5/2	5/2	-2	2
BS7	4.50	1	-5/2	5/2	2	3
BS8	8.11	1	2	-5/2	5/2	3
BS9	5.11	1	5/2	2	-5/2	3
BS10	16.75	1	-2	5/2	5/2	4
BS11	18.57	1	5/2	-2	5/2	4
BS12	18.77	1	5/2	5/2	-2	4
BS13	22.54	-1	5/2	5/2	2	6
HS	33.67	1	5/2	5/2	2	8

Table S7. BS-DFT-calculated spin ladder to fit the Heisenberg exchange Hamiltonian for $NiFd_{ox}$.

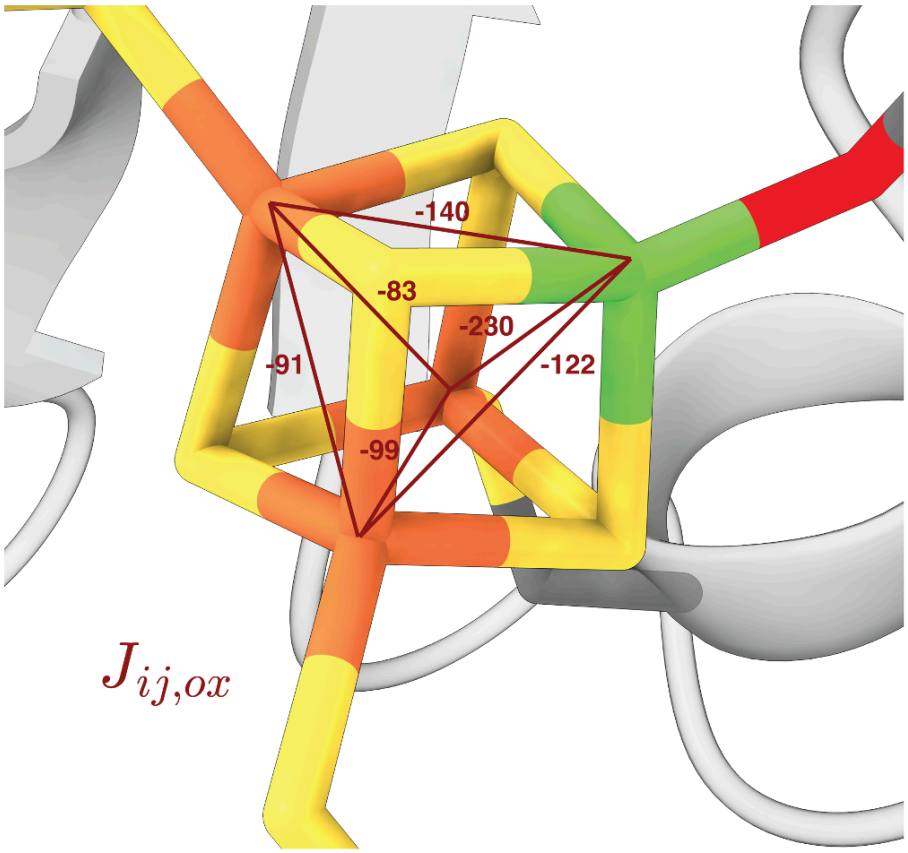

Figure S39. Computed Ni-Fe Heisenberg exchange couplings for $NiFd_{ox}$ computed using the spin ladder in **Table S5**.

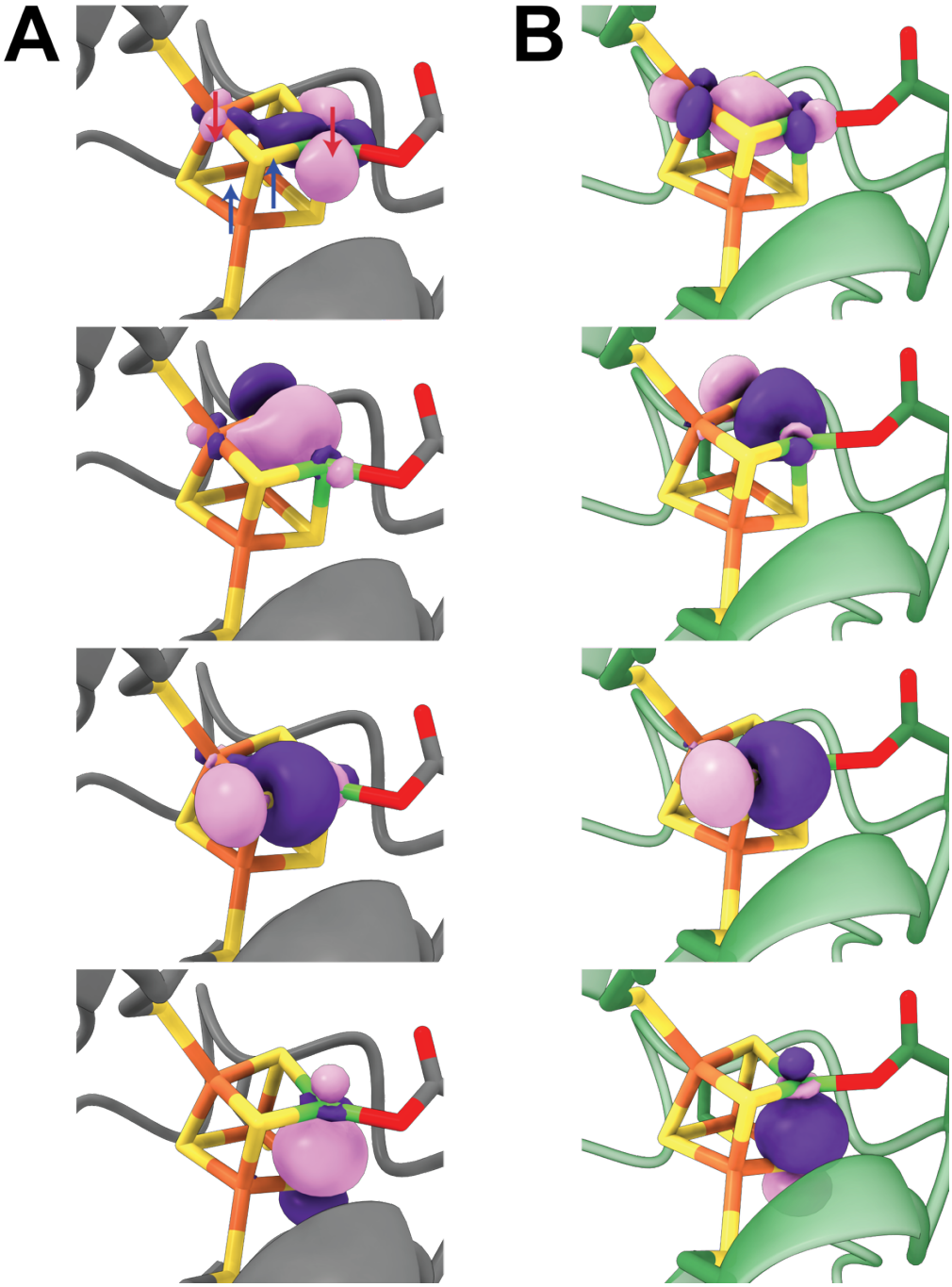

Figure S40. Pipek-Mezey localized orbitals with Ni contribution for the lowest energy broken-symmetry states of (A) $NiFd_{ox}$ and (B) $NiFd_{red}$, localized over the α density. Arrows are shown for the first orbital in (A) to indicate the Ni-Fe pair that is ferromagnetically coupled in the BS-DFT spin density (state BS3). A contour value of 0.05 was used for visualization.

Discussion of Ni-Fe bonding analysis

To determine the nature of a possible Ni-Fe bond, we first used Quantum Theory of Atoms in Molecules (QTAIM) to probe the charge density of $NiFd_{ox}$ and $NiFd_{red}$.[15,16] QTAIM provides an overlap of a ring critical point (formed by the Ni-S and Fe-S bond critical points) and where a Ni-Fe bond critical point could exist does not entirely exclude the possibility of a bonding interaction. We extended our analysis further to Pipek-Mezey localization of the broken-symmetry states of $NiFd_{ox}$ and $NiFd_{red}$, and observed a bonding-like orbital (**Figure S40**), solely corresponding to the Ni and Fe that are ferromagnetically coupled, and only appearing in the α channel. This contrasts with previous work from the Holland group, where the orbitals were in both α/β-channels, which implies that the orbitals observed here are the ferromagnetic exchange coupling rather than two-electron bonding orbitals. Additional localized orbitals were observed corresponding to Ni-S bonding (**Figure S40**) that displayed Fe d-character, which can be attributed to the sulfides being exchange mediators.

We further analyzed the bonding by computing Wiberg-Mayer bond indices, which yielded Ni-Fe bond indices of c.a. 0.05.[17] Typical covalent single bonds have bond indices of ~1.0, and for $NiFd_{ox}$ and $NiFd_{red}$ the Ni-S bonds and Fe-S bonds had bond indices of c.a. 0.5, showing that the Ni-Fe bond indices are negligible. Lastly, we utilized JANPA to compute localized property-optimized orbitals, which compute bonding orbitals in a similar manner to natural bonding orbitals.[18] This procedure yielded zero bonding orbitals between any Ni-Fe pair for both $NiFd_{ox}$ and $NiFd_{red}$ across the broken-symmetry states. Overall, the computational analysis does not give any clear indication of Ni-Fe bonding.

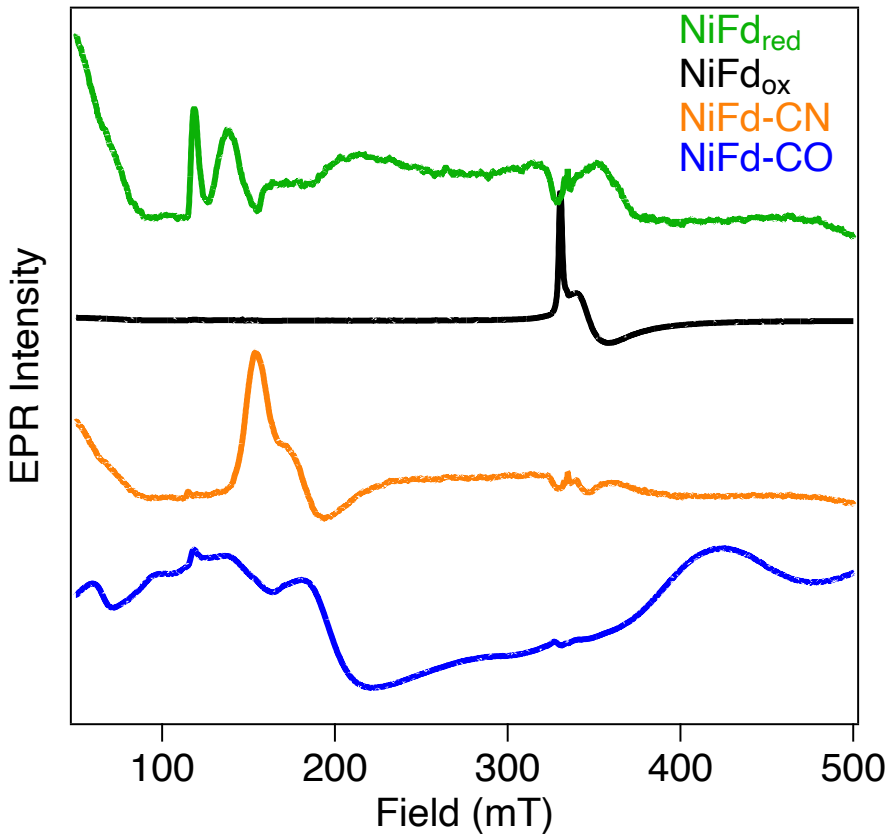

Figure S41. CW EPR spectra (ν = 9.36 GHz, T = 5 K, $P_{\mu W}$ = 20 mW) for HERFD XAS samples of $NiFd_{red}$ (*green*), $NiFd_{ox}$ (*black*), NiFd-CN (*orange*), and NiFd-CO (*blue*). $NiFd_{red}$, $NiFd_{ox}$, NiFd-CN include 30% v/v glycerol; NiFd-CO has no glassing agent. The irregular baseline for NiFd-CO is due to underfilling the EPR instrument cavity to preserve sample amount and concentration.

References

(1) Stoll, S.; Schweiger, A. EasySpin, a Comprehensive Software Package for Spectral Simulation and Analysis in EPR. *J. Magn. Reson.* **2006**, *178* (1), 42–55. https://doi.org/10.1016/j.jmr.2005.08.013.

(2) Conover, R. C.; Park, J. B.; Adams, M. W. W.; Johnson, M. K. Formation and Properties of an Iron-Nickel Sulfide (NiFe3S4) Cluster in Pyrococcus Furiosus Ferredoxin. *J. Am. Chem. Soc.* **1990**, *112* (11), 4562–4564. https://doi.org/10.1021/ja00167a074.

(3) Lewis, L. C.; Shafaat, H. S. Reversible Electron Transfer and Substrate Binding Support [NiFe $_3$ S $_4$] Ferredoxin as a Protein-Based Model for [NiFe] Carbon Monoxide Dehydrogenase. *Inorg. Chem.* **2021**, *60* (18), 13869–13875. https://doi.org/10.1021/acs.inorgchem.1c01323.

(4) Lewis, L. C. Electronic Isomerism in a Heterometallic Nickel–Iron–Sulfur Cluster Models Substrate Binding and Cyanide Inhibition of Carbon Monoxide Dehydrogenase. *Chem Sci* **2024**.

(5) Kent, T. A.; Huynh, B. H.; Münck, E. Iron-Sulfur Proteins: Spin-Coupling Model for Three-Iron Clusters. *Proc. Natl. Acad. Sci.* **1980**, *77* (11), 6574–6576. https://doi.org/10.1073/pnas.77.11.6574.

(6) Brown, A. C.; Suess, D. L. M. An Open-Cuboidal [Fe3S4] Cluster Characterized in Both Biologically Relevant Redox States. *J. Am. Chem. Soc.* **2023**, *145* (4), 2075–2080. https://doi.org/10.1021/jacs.2c13126.

(7) Boudalis, A. K. Half-Integer Spin Triangles: Old Dogs, New Tricks. *Chem. – Eur. J.* **2021**, *27* (24), 7022–7042. https://doi.org/10.1002/chem.202004919.

(8) Wilson, D. W. N.; Fataftah, M. S.; Mathe, Z.; Mercado, B. Q.; DeBeer, S.; Holland, P. L. Three-Coordinate Nickel and Metal–Metal Interactions in a Heterometallic Iron–Sulfur Cluster. *J. Am. Chem. Soc.* **2024**, *146* (6), 4013–4025. https://doi.org/10.1021/jacs.3c12157.

(9) Fataftah, M. S.; Wilson, D. W. N.; Mathe, Z.; Gerard, T. J.; Mercado, B. Q.; DeBeer, S.; Holland, P. L. Inserting Three-Coordinate Nickel into [4Fe-4S] Clusters. *ACS Cent. Sci.* **2024**, *10* (10), 1910–1919. https://doi.org/10.1021/acscentsci.4c00985.

(10) Srivastava, K. K. P.; Surerus, K. K.; Conover, R. C.; Johnson, M. K.; Park, J. B.; Adams, M. W. W.; Munck, E. Moessbauer Study of Zinc-Iron-Sulfur ZnFe3S4 and Nickel-Iron-Sulfur NiFe3S4 Clusters in Pyrococcus Furiosus Ferredoxin. *Inorg. Chem.* **1993**, *32* (6), 927–936. https://doi.org/10.1021/ic00058a029.

(11) Huynh, B. H.; Moura, J. J.; Moura, I.; Kent, T. A.; LeGall, J.; Xavier, A. V.; Münck, E. Evidence for a Three-Iron Center in a Ferredoxin from Desulfovibrio Gigas. Mössbauer and EPR Studies. *J. Biol. Chem.* **1980**, *255* (8), 3242–3244.

(12) Papaefthymiou, V.; Girerd, J. J.; Moura, I.; Moura, J. J. G.; Muenck, E. Moessbauer Study of D. Gigas Ferredoxin II and Spin-Coupling Model for Fe3S4 Cluster with Valence Delocalization. *J. Am. Chem. Soc.* **1987**, *109* (15), 4703–4710. https://doi.org/10.1021/ja00249a037.

(13) Finnegan, M. G.; Conover, R. C.; Park, J.-B.; Zhou, Z. H.; Adams, M. W. W.; Johnson, M. K. Electronic, Magnetic, Redox, and Ligand-Binding Properties of [MFe3S4] Clusters (M = Zn, Co, Mn) in Pyrococcus Furiosus Ferredoxin. *Inorg. Chem.* **1995**, *34* (21), 5358–5369. https://doi.org/10.1021/ic00125a040.

(14) Girerd, J.-J.; Papaefthymiou, V.; Surerus, K. K.; Munck, E. Double Exchange in Iron-Sulfur Clusters and a Proposed Spin-Dependent Transfer Mechanism. *Pure Appl. Chem.* **1989**, *61* (5), 805–816. https://doi.org/10.1351/pac198961050805.

(15) Lu, T. A Comprehensive Electron Wavefunction Analysis Toolbox for Chemists, Multiwfn. *J. Chem. Phys.* **2024**, *161* (8), 082503. https://doi.org/10.1063/5.0216272.
(16) Bader, R. F. W. A Quantum Theory of Molecular Structure and Its Applications. *Chem. Rev.* **1991**, *91* (5), 893–928. https://doi.org/10.1021/cr00005a013.
(17) Mayer, I. Bond order and valence indices: A personal account. *J. Comput. Chem.* **2007**, *28* (1), 204–221. https://doi.org/10.1002/jcc.20494.
(18) Nikolaienko, T. Y.; Bulavin, L. A. Localized Orbitals for Optimal Decomposition of Molecular Properties. *Int. J. Quantum Chem.* **2019**, *119* (3), e25798. https://doi.org/10.1002/qua.25798.